

VYSOKÉ UČENÍ TECHNICKÉ V BRNĚ

BRNO UNIVERSITY OF TECHNOLOGY

FAKULTA STROJNÍHO INŽENÝRSTVÍ
ÚSTAV FYZIKÁLNÍHO INŽENÝRSTVÍ

FACULTY OF MECHANICAL ENGINEERING
INSTITUTE OF PHYSICAL ENGINEERING

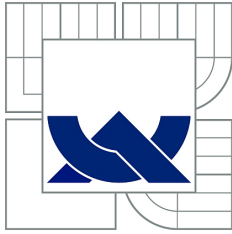
MĚŘENÍ EXTINKČNÍCH SPEKTER OPTICKY ZACHYCENÝCH
PLAZMONICKÝCH NANOČÁSTIC

DIPLOMOVÁ PRÁCE
MASTER'S THESIS

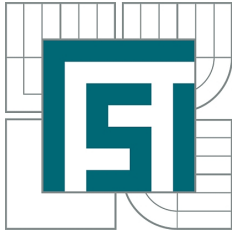
AUTOR PRÁCE
AUTHOR

Bc. JANA DAMKOVÁ

BRNO 2015



BRNO UNIVERSITY OF TECHNOLOGY
VYSOKÉ UČENÍ TECHNICKÉ V BRNĚ



FACULTY OF MECHANICAL ENGINEERING
INSTITUTE OF PHYSICAL ENGINEERING
FAKULTA STROJNÍHO INŽENÝRSTVÍ
ÚSTAV FYZIKÁLNÍHO INŽENÝRSTVÍ

MEASUREMENT OF EXTINCTION SPECTRA OF
OPTICALLY TRAPPED PLASMON NANO-PARTICLES
MĚŘENÍ EXTINKČNÍCH SPEKTER OPTICKY ZACHYCENÝCH PLAZMONICKÝCH
NANOČÁSTIC

MASTER'S THESIS
DIPLOMOVÁ PRÁCE

AUTHOR
AUTOR PRÁCE

Bc. JANA DAMKOVÁ

SUPERVISOR
VEDOUcí PRÁCE

Mgr. OTO BRZOBOHATÝ, Ph.D.

BRNO 2015

Vysoké učení technické v Brně, Fakulta strojního inženýrství

Ústav fyzikálního inženýrství

Akademický rok: 2014/2015

ZADÁNÍ DIPLOMOVÉ PRÁCE

student(ka): Bc. Jana Damková

který/která studuje v **magisterském navazujícím studijním programu**

obor: **Fyzikální inženýrství a nanotechnologie (3901T043)**

Ředitel ústavu Vám v souladu se zákonem č.111/1998 o vysokých školách a se Studijním a zkušebním řádem VUT v Brně určuje následující téma diplomové práce:

Měření extinkčních spekter opticky zachycených plazmonických nanočástic

v anglickém jazyce:

Measurement of extinction spectra of optically trapped plasmon nano-particles

Stručná charakteristika problematiky úkolu:

Zlaté a stříbrné nanočástice jsou velmi důležité v různých nanooptických aplikacích, například u povrchově zesílené Ramanovy spektroskopie (SERS), rastrovací optické mikroskopie blízkého pole (SNOM) nebo v nanofotonických zařízeních. Jejich zajímavé optické vlastnosti vycházejí z lokalizované povrchové plazmonové rezonance, což jsou kolektivní oscilace vodivostních elektronů vybuzené po ozáření elektromagnetickým polem. Zlato a stříbro vykazují tyto oscilace ve viditelném oboru a jejich frekvence silně závisí na tvaru a velikosti nanočástice.

Cíle diplomové práce:

Úkolem diplomové práce je měření optické odezvy samostatně opticky zachycených nanočástic různých tvarů a velikostí. Pro optické zachycení bude využita dnes již rutinně používaná optická pinzeta. Částice bude osvětlena osvittem temného pole a rozptýlené pole bude snímáno spektrometrem. Takto získaná spektra mohou být srovnána s teoretickými výpočty, získanými volně dostupnými výpočetními programy (např. ADDA).

ABSTRACT

This thesis deals with the dark-field imaging and the optical spectroscopy of optically trapped plasmonic nanoparticles. The optical trapping and the characterization of a single particle or multiple nanoparticles as well are demonstrated. The number of the optically trapped particles can be estimated from the dark-field scattering intensity. Experiments show the presence of the interparticle coupling among trapped metallic nanoparticles which has not been observed in case of dielectric particles. The scattering spectra of the plasmonic nanoparticles were compared with theoretical models based on the Mie theory and the Discrete dipole approximation.

KEYWORDS

optical spectroscopy, optical tweezers, dark field, metallic nanoparticles, scattering, ADDA, Mie theory

ABSTRAKT

Tato práce se zabývá zobrazováním v temném poli a optickou spektroskopií opticky zachycených plazmonických nanočástic. Optické chytání a charakterizace jednotlivých částic nebo jejich určitého množství jsou názorně vysvětleny. Počet opticky chycených částic může být odhadnut z intenzity rozptylu objektu v temném poli. Experimenty prokazují u chycených kovových nanočástic jejich vzájemnou interakci, na rozdíl od částic dielektrických. Rozptylová spektra plazmonických nanočástic jsou srovnána s teoretickými modely založenými na Mieho teorii a Diskrétní dipólové aproximaci.

KLÍČOVÁ SLOVA

optická spektroskopie, optická pinzeta, temné pole, kovové nanočástice, rozptyl, ADDA, Mieho teorie

DAMKOVÁ, Jana *Měření extinkčních spekter opticky zachycených plazmonických nanočástic*: diplomová práce. Brno: Vysoké učení technické v Brně, Fakulta strojního inženýrství, Ústav fyzikálního inženýrství, 2015. 63 s. Vedoucí práce Mgr. Oto Brzobohatý, Ph.D.

PROHLÁŠENÍ

Prohlašuji, že svou diplomovou práci na téma „Měření extinkčních spekter opticky zachycených plazmonických nanočástic“ jsem vypracovala samostatně pod vedením vedoucího diplomové práce a s použitím odborné literatury a dalších informačních zdrojů, které jsou všechny citovány v práci a uvedeny v seznamu literatury na konci práce.

Jako autorka uvedené diplomové práce dále prohlašuji, že v souvislosti s vytvořením této diplomové práce jsem neporušila autorská práva třetích osob, zejména jsem nezasáhla nedovoleným způsobem do cizích autorských práv osobnostních a jsem si plně vědoma následků porušení ustanovení § 11 a následujících autorského zákona č. 121/2000 Sb., včetně možných trestněprávních důsledků vyplývajících z ustanovení § 152 trestního zákona č. 140/1961 Sb.

Brno

.....

(podpis autora)

Acknowledgements

I thank my supervisor Mgr. Oto Brzobohatý, Ph.D. for scientific guidance through the work, introducing me to the optics, help with the experiment realizations and assistance with ADDA simulations. I thank prof. RNDr. Pavel Zemánek, Ph.D. for giving me the opportunity to join Optical Micro-manipulation Techniques group at the Institute of Scientific Instruments of the CAS. Thanks to all group members from the group for their helpful suggestions. I thank Mgr. Jindřich Oulehla for the fabrication of the dielectric mirror and Ing. Filip Novotný for the synthesis of gold nanoparticles. My gratitude also belongs to members of Department of Physical Engineering at FME BUT who were always ready to help. My thanks goes to my parents and Lukáš for their support and love.

CONTENTS

1	Introduction	3
2	Theoretical background	5
2.1	Theory of the electromagnetic field	5
2.2	Drude model	7
2.3	The field scattered by small metallic particles	8
2.3.1	Quasi-static approximation	10
2.3.2	Mie theory	13
2.3.3	Discrete dipole approximation	16
2.3.4	Size and shape effects	20
3	Spectroscopy of optically trapped particles	25
3.1	Experimental techniques	25
3.1.1	Optical trapping	25
3.1.2	Köhler dark-field illumination	29
3.1.3	Experimental setup	32
3.2	Characterization of nanoparticle scattering	36
3.2.1	Setup alignment using polystyrene particles	36
3.2.2	The light scattered by silver nanoparticles	40
3.2.3	Optical spectroscopy of gold nanoparticles	46
4	Conclusions	53
	Bibliography	55
	List of Abbreviations	63

1 INTRODUCTION

Extraordinary light–matter interactions in metallic structures form a new branch in nanophotonics called plasmonics. This field of science deals with the generation, manipulation, guiding and transportation of electromagnetic waves in metals at the nanoscale. It is based on the interaction between the electromagnetic radiation and collective oscillations of conductive electrons in metals, so called plasmons. We distinguish two main types of these oscillations: surface plasmon polaritons (SPPs) and localized surface plasmon polaritons (LSPPs). SPPs are electromagnetic surface waves of the charge density interacting with the incident electromagnetic wave that exist at the metal–dielectric interface. They were predicted by R. H. Ritchie in 1957 [1] and three years later they were experimentally verified [2]. The second group, LSPPs, represents oscillations of electrons in metallic nanoparticles. The application of metallic nanoparticles is dated back to Roman times when the nanoparticles were used for example in the staining of glass in ornamental windows or in Lycurgus cup [3]. The clear mathematical foundation for these oscillations was established by G. Mie in 1908 [4].

The electromagnetic field around metallic nanoparticles can be strongly enhanced and highly confined on a scale much smaller than the wavelength of the incident light due to plasmon oscillations [5]. Particles that enhance and confine electromagnetic fields in their vicinities are called nanoantennas. Up to now, nanoparticles of different shapes and materials have been studied, for example spheres [6, 7], nanorods [8, 9], triangles [7, 10], discs [11, 12] and decahedrons [10, 13] fabricated from gold [10, 14], silver [15, 16] or palladium [17, 18].

Plasmonic nanoparticles are widely used for Surface-Enhanced Raman Scattering (SERS) [19, 20], Surface-Enhanced Infrared Absorption Spectroscopy (SEIRA) [21], Single-Molecule Raman Spectroscopy [22], infrared detectors [23], biosensors [24, 25] and boosting fluorescence [26, 27]. Apart from a basic research in plasmonics, nanoantennas have applications in the areas of medicine for labeling macromolecules [28, 29], optoelectronics [30, 31], telecommunications [32, 33], microscopy [34, 35], spectroscopy [36, 37] and many others.

The progress in nanotechnology and state-of-the-art techniques enable to fabricate desired nanoparticles [38] and to theoretically and experimentally investigate their properties. For nanoparticles utilization, there is a clear demand for their optimized characteristics, as localized-surface-plasmon (LSP) resonances of nanoparticles. In some applications, only a single particle is used for the field enhancement or sensing, e. g. SERS or biosensing. Therefore the investigation of the optical properties of a single isolated nanoparticle is desired. This can be provided by optical trapping of a single nanoparticle in a solution using a focused laser beam, so called optical

tweezers [39], and the dark-field illumination for the nanoparticle spectroscopy.

In this thesis we deal with the dark-field imaging and the optical spectroscopy of metallic nanoparticles. In order to have a possibility to investigate just a single nanoparticle from a colloidal solution or a desired number of them, we implemented into an optical setup an optical tweezers that enables to trap a particle by a focused light beam. Nanoparticles in an aqueous solution were illuminated by the dark-field illumination and then only the light scattered by the nanoparticle could be recorded. The chosen particle from the colloidal solution was optically trapped and thus the scattering spectrum could be recorded for a desired time. So this technique should allow us to record scattering spectra of nanoparticles even with a lower scattering intensity. The scattering spectra of metallic nanoparticles were also obtained through the theoretical calculations using the Mie theory and the Discrete dipole approximation (DDA).

This thesis is organized as follows; in chapter 2 we present basics of the electromagnetic-field theory. Afterwards, the Drude model for the dielectric-function description is explained. Then we introduce the theory for the field scattered by a small particle. We show basic principles of the quasi-static approximation, the Mie theory and also the numerical calculations that we used for the optical characterization of plasmonic particles. At the end of this chapter we discuss an influence of the particle size and its shape on the scattered field. In chapter 3 we describe details of the experimental setup used for the particle spectroscopy consisting of optical tweezers, Köhler dark-field illumination and an optical branch for a detection and a characterization of the scattered light. Then we study nanoparticle scattering, both experimentally and theoretically. For the setup alignment we use polystyrene particles and consequently scattering spectra of silver and gold nanoparticles are discussed. Finally, in chapter 4 we summarize this work and give an outlook on the further studies.

2 THEORETICAL BACKGROUND

The presented work deals with metallic nanoparticles in an aqueous solution and investigates their scattered field by dark-field microscopy using optical tweezers. In this chapter, an introduction to the theoretical description of the electromagnetic field is given. At the beginning of the chapter, we deal with Maxwell's equations and the dielectric function that is necessary for the characterization of optical properties of materials. Further we present two analytical descriptions of the scattered field of metallic particles and the basic principle of the Discrete dipole approximation for numerical calculations of the scattered field is described. At the end of this chapter the effects of particle sizes and shapes on the scattering process are discussed.

2.1 Theory of the electromagnetic field

The electromagnetic field can be described by the macroscopic Maxwell's equations [40, p. 12]

$$\nabla \cdot \mathbf{D} = \rho_{\text{F}}, \quad (2.1\text{a})$$

$$\nabla \cdot \mathbf{B} = 0, \quad (2.1\text{b})$$

$$\nabla \times \mathbf{E} = -\frac{\partial \mathbf{B}}{\partial t}, \quad (2.1\text{c})$$

$$\nabla \times \mathbf{H} = \mathbf{J}_{\text{F}} + \frac{\partial \mathbf{D}}{\partial t}, \quad (2.1\text{d})$$

where ρ_{F} is the density of free charges, \mathbf{B} is the magnetic induction, \mathbf{E} is the electric field, t is time and \mathbf{J}_{F} is the free current density. The electric displacement \mathbf{D} and the magnetic field \mathbf{H} are defined by the following expressions [40, p. 12]:

$$\mathbf{D} = \varepsilon_0 \mathbf{E} + \mathbf{P}, \quad (2.2\text{a})$$

$$\mathbf{H} = \frac{\mathbf{B}}{\mu_0} - \mathbf{M}, \quad (2.2\text{b})$$

where ε_0 is the vacuum permittivity, \mathbf{P} is the electric polarization (mean value of the electric dipole moment per unit volume), \mathbf{M} is the magnetization (mean value of the magnetic dipole moment per unit volume) and μ_0 is the vacuum permeability.

If the medium is linear, isotropic and nonmagnetic, vectors \mathbf{E} and \mathbf{D} are parallel, as well vectors \mathbf{B} and \mathbf{H} , and they are linked via [41, p. 189]

$$\mathbf{D} = \varepsilon \mathbf{E}, \quad (2.3\text{a})$$

$$\mathbf{H} = \frac{1}{\mu} \mathbf{B}, \quad (2.3\text{b})$$

where ε is the electric permittivity and μ is the magnetic permeability of the medium.

After inserting Eqs. (2.3) into Eqs. (2.2) we obtain [41, p. 189]

$$\mathbf{P} = \varepsilon_0 \chi_e \mathbf{E}, \quad (2.4a)$$

$$\mathbf{M} = \chi_m \mathbf{H}. \quad (2.4b)$$

The electric susceptibility χ_e and the magnetic susceptibility χ_m are given by

$$\chi_e = \frac{\varepsilon}{\varepsilon_0} - 1 = \varepsilon_r - 1, \quad (2.5a)$$

$$\chi_m = \frac{\mu}{\mu_0} - 1 = \mu_r - 1, \quad (2.5b)$$

where ε_r and μ_r correspond to the relative permittivity and the relative permeability, respectively.

Let us consider the harmonic time dependence of the fields [40, p. 25]

$$\mathbf{E}(\mathbf{r}, t) = \text{Re} \{ \mathbf{E}_0 \exp [i(\mathbf{k} \cdot \mathbf{r} - \omega t)] \}, \quad (2.6a)$$

$$\mathbf{H}(\mathbf{r}, t) = \text{Re} \{ \mathbf{H}_0 \exp [i(\mathbf{k} \cdot \mathbf{r} - \omega t)] \}, \quad (2.6b)$$

in linear, isotropic and nonmagnetic medium ($\nabla \varepsilon = \mathbf{0}$ and $\nabla \mu = \mathbf{0}$) without free charges and free currents ($\rho_F = 0$ and $\mathbf{J}_F = \mathbf{0}$). \mathbf{E}_0 and \mathbf{H}_0 represent the amplitudes of the electric field and the magnetic field, respectively, i is the imaginary unit, \mathbf{r} is the position vector, ω is the angular frequency, \mathbf{k} is the wave vector and from Maxwell's equations (2.1) $\mathbf{k} \perp \mathbf{E}$ and $\mathbf{k} \times \mathbf{E} = \omega \mathbf{H}$. Using Maxwell's equations (2.1) we can derive the Helmholtz equation [42, p. 296]

$$(\nabla^2 + k^2) \begin{Bmatrix} \mathbf{E} \\ \mathbf{H} \end{Bmatrix} = \mathbf{0}. \quad (2.7)$$

Solving Maxwell's equations for a boundary of two different media we arrive at the boundary conditions [43]

$$(\mathbf{D}_2 - \mathbf{D}_1) \cdot \mathbf{n} = \sigma_F, \quad (2.8a)$$

$$(\mathbf{B}_2 - \mathbf{B}_1) \cdot \mathbf{n} = 0, \quad (2.8b)$$

$$\mathbf{n} \times (\mathbf{E}_2 - \mathbf{E}_1) = \mathbf{0}, \quad (2.8c)$$

$$\mathbf{n} \times (\mathbf{H}_2 - \mathbf{H}_1) = \mathbf{K}_F, \quad (2.8d)$$

where σ_F is the surface density of free charges and \mathbf{K}_F is the surface free current density, \mathbf{n} is the normal vector oriented as in Fig. 2.1 and other notation is apparent from Fig. 2.1.

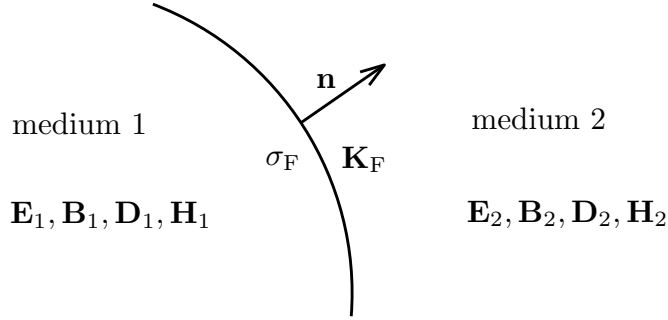


Fig. 2.1: Notation of the field quantities at a boundary of two different media; adapted from [43].

2.2 Drude model

Optical properties of materials are described by their relative permittivities. The relative permittivities are generally functions of the angular frequencies of the incident electromagnetic waves thus they are often called dielectric functions. In 1900 Drude proposed a model for the description of the optical response of the conduction electrons in metals. He supposed that electrically positive ions form a fixed crystal lattice and conduction electrons can move freely. Thus the metal materials with the low damping have similar optical properties as plasma. The damping γ is mainly caused by scattering of conduction electrons on lattice vibrations (phonons) and is defined as $\gamma = 1/\tau$, where τ is the electronic scattering time. The equation for motion of an electron is [40, p. 251]

$$m_e \ddot{\mathbf{x}} + m_e \gamma \dot{\mathbf{x}} = -e \mathbf{E}, \quad (2.9)$$

where m_e is the electron mass, \mathbf{x} is the displacement from the equilibrium position, e is the magnitude of the electron charge and the dot above the symbol means time derivation. Supposing harmonic time dependence of the electric field with the angular frequency ω , the solution of Eq. (2.9) is of the form

$$\mathbf{x}(t) = \frac{e}{m_e} \frac{1}{\omega^2 + i\gamma\omega} \mathbf{E}(t). \quad (2.10)$$

Conduction electrons are displaced by the external electric field \mathbf{E} with respect to the ion lattice and thus the material is polarized (the dipole moment of one electron $\mathbf{p} = -e\mathbf{x}$). Via the density of free electrons \mathcal{N} we can obtain the electric polarization

$$\mathbf{P}(t) = \mathcal{N} \mathbf{p}(t) = -\mathcal{N} e \mathbf{x}(t) = -\frac{\mathcal{N} e^2}{m_e (\omega^2 + i\gamma\omega)} \mathbf{E}(t). \quad (2.11)$$

Comparing Eq. (2.11) with Eq. (2.4a) and accounting Eq. (2.5a) we get the expression for the dielectric function

$$\varepsilon_r(\omega) = 1 - \frac{\omega_p^2}{\omega^2 + i\gamma\omega}, \quad (2.12)$$

where we introduced the plasma frequency

$$\omega_p = \sqrt{\frac{\mathcal{N}e^2}{m_e \epsilon_0}}. \quad (2.13)$$

The plasma frequency is the resonant frequency of the charge motion in the plasma which consists of free electrons and positive ions. These oscillations can be described by the same model as applies for metals supposing $\gamma \rightarrow 0$.

Apart from free electrons, also bound electrons have a substantial effect on the profile of the dielectric function; for example in gold a bound-electron contribution to the dielectric function dominates at resonant frequencies [40, p. 337] (discussed later in section 2.3.1). Therefore we have to add to the dielectric function derived by the Drude model ϵ_r^D (Eq. (2.12)) Lorentzian terms ϵ_r^L where a restoring force is included [40, p. 258]:

$$\epsilon_r(\omega) = \epsilon_r^D(\omega) + \epsilon_r^L(\omega) = 1 - \frac{\omega_p^2}{\omega^2 + i\gamma\omega} + \sum_j \frac{\omega_{pj}^2}{\omega_j^2 - \omega^2 - i\gamma_j\omega}, \quad (2.14)$$

where ω_{pj} is the oscillator plasma frequency, ω_j is the oscillator resonant frequency and γ_j is its damping constant.

2.3 The field scattered by small metallic particles

To explain the scattering process we consider an object which consists of electrons and electrically positive ions. If the object is illuminated by an incident electromagnetic wave, charges can start to oscillate. The oscillatory motion of charges driven by the external electromagnetic field causes the emission of the radiation of the electromagnetic field in all directions. This radiation is called the radiation scattered by the object [40, p. 3] and the whole process consists of the excitation and the reradiation.

We distinguish two types of scattering of the incident light, elastic and inelastic. In the elastic scattering (Rayleigh scattering [40, p. 7]) the frequency of the scattered light is the same as the frequency of the incident light. If the energy of the emitted photon is different from the energy of the absorbed one, the scattering is inelastic (Raman scattering [44]).

Except the reradiation of the energy of the excited charges, the energy can be transformed into other forms, for example thermal energy. This energy-dissipation process is called absorption and always appears simultaneously with the electromagnetic-field scattering. The sum of scattering and absorption is generally called extinction. The magnitude of the extinction depends on dielectric functions of the

studied object and its surrounding medium, its size, shape, orientation, the presence of other particles and on the polarization and the frequency of the incident electromagnetic field.

For quantitative description of scattering and absorption of the incident field, it is necessary to examine the flux of the Poynting vector \mathbf{S} [40, p. 63]

$$\mathbf{S} = \frac{1}{\mu_0} (\mathbf{E} \times \mathbf{B}). \quad (2.15)$$

If we consider a sphere surrounding the studied particle, the rate of the energy transmission through the sphere with the surface A is [40, p. 69]

$$W_{\text{abs}} = - \int_A \mathbf{S} \cdot \mathbf{e}_r \, dA, \quad (2.16)$$

where \mathbf{e}_r is the unit vector in the radial direction. The energy entering the sphere space is positive and the energy leaving the space is negative. It is evident that W_{abs} represents the energy absorption rate. If the energy is absorbed by the particle, it always applies $W_{\text{abs}} > 0$. W_{abs} can be written as the sum of three terms [40, p. 70]:

$$W_{\text{abs}} = W_{\text{i}} - W_{\text{sca}} + W_{\text{ext}}, \quad (2.17)$$

where

$$W_{\text{i}} = - \int_A \mathbf{S}_{\text{i}} \cdot \mathbf{e}_r \, dA, \quad W_{\text{sca}} = \int_A \mathbf{S}_{\text{sca}} \cdot \mathbf{e}_r \, dA, \quad W_{\text{ext}} = - \int_A \mathbf{S}_{\text{ext}} \cdot \mathbf{e}_r \, dA \quad (2.18)$$

and the indices i, sca and ext denote the incident light, the scattered light and the extinction, respectively. For a nonabsorbing medium, i.e. $W_{\text{i}} = 0$, we arrive at the relationship

$$W_{\text{ext}} = W_{\text{abs}} + W_{\text{sca}}. \quad (2.19)$$

The ratio of W_{ext} to the incident irradiance I_{i} is the so called extinction cross section C_{ext} , the quantity with dimensions of area:

$$C_{\text{ext}} = \frac{W_{\text{ext}}}{I_{\text{i}}}. \quad (2.20)$$

Following Eq. (2.19), C_{ext} is a sum of the absorption cross section C_{abs} and the scattering cross section C_{sca} :

$$C_{\text{ext}} = C_{\text{abs}} + C_{\text{sca}}, \quad (2.21)$$

where

$$C_{\text{abs}} = \frac{W_{\text{abs}}}{I_{\text{i}}}, \quad C_{\text{sca}} = \frac{W_{\text{sca}}}{I_{\text{i}}}. \quad (2.22)$$

The extinction cross section can have a different value from the geometrical cross section of the particle. For instance gold nanoparticles can have severalfold larger extinction cross sections than their real geometrical cross sections [45, 60].

There are several ways how to determine scattered field of a particle. The simplest one is the quasi-static approximation. This approximation is valid for particles much smaller than the wavelength of the incident light. Retardation effect can be neglected and the particle behaves like an oscillating dipole. As the size of the particle increases, the particle is not polarized homogeneously and higher-order modes are now important. For spherical and ellipsoidal particle, Mie theory can be used for the description of the scattered field. In other geometries, numerical methods are required for solving of Maxwell's equations, for example Discrete dipole approximation (DDA). These three different approaches how to characterize the scattered field are described in more details in the following sections.

2.3.1 Quasi-static approximation

In this section, we analyse the scattered field of a metallic nanosphere with a radius $a \ll \lambda$ (λ is a wavelength of the incident light.), for a gold particle in an aqueous solution $2a < 25$ nm [8]. We can assume that the external electric field has the constant phase over the whole nanoparticle volume and therefore the problem is reduced to the electrostatic one. The nanoparticle behaves under the incident light like an oscillating electric point dipole \mathbf{p} (see Fig. 2.2) and the field outside of the nanosphere can be described as a superposition of the external field and the field of a point dipole located in the center of the nanosphere. This description of the scattered field of a nanoparticle is called quasi-static approximation. The derivation showed in this section follows the one presented in [46, p. 66].

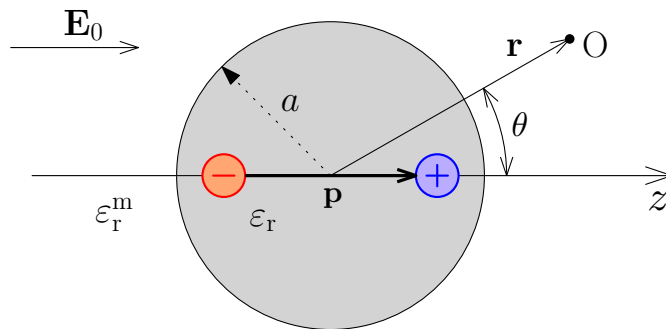


Fig. 2.2: Scheme of a nanosphere placed into an electrostatic field \mathbf{E}_0 ; adapted from [46].

To find the distribution of the electric field around the nanosphere, we have to deal with the Laplace equation for the electric potential

$$\nabla^2\Phi = 0, \tag{2.23}$$

where the electric field is given by

$$\mathbf{E} = -\nabla\Phi. \quad (2.24)$$

Due to the azimuthal symmetry, the general solution is of the form

$$\Phi(r, \theta) = \sum_{l=0}^{\infty} (A_l r^l + B_l r^{-l-1}) P_l(\cos \theta), \quad (2.25)$$

where r is the distance from the dipole to the point O where the field is studied, θ is the angle between the position vector \mathbf{r} and the z axis, A_l and B_l are the coefficients obtained from the boundary conditions and $P_l(\cos \theta)$ are the Legendre polynomials of the order l .

The solution for the electric potential inside Φ_{in} and outside Φ_{out} the nanosphere is determined from the boundary conditions (for $r \rightarrow \infty$: $\Phi_{\text{out}} \rightarrow -E_0 r \cos \theta$ and Eqs. (2.8))

$$\Phi_{\text{in}} = -\frac{3\varepsilon_r^{\text{m}}}{\varepsilon_r + 2\varepsilon_r^{\text{m}}} E_0 r \cos \theta, \quad (2.26a)$$

$$\Phi_{\text{out}} = -E_0 r \cos \theta + \frac{\mathbf{p} \cdot \mathbf{r}}{4\pi\varepsilon_0\varepsilon_r^{\text{m}}r^3}, \quad (2.26b)$$

where ε_r^{m} is the dielectric function outside the nanosphere, ε_r is the dielectric function of the nanoparticle, E_0 is the amplitude of the applied electric field and \mathbf{p} represents the electrostatic dipole moment of the nanoparticle of the form

$$\mathbf{p} = 4\pi\varepsilon_0\varepsilon_r^{\text{m}}a^3 \frac{\varepsilon_r - \varepsilon_r^{\text{m}}}{\varepsilon_r + 2\varepsilon_r^{\text{m}}} \mathbf{E}_0, \quad (2.27)$$

where a is the radius of the nanosphere. We see from Eq. (2.26b) that the potential outside the nanosphere is given by a sum of the external potential (the first term) and the potential of the electric dipole induced by the external field (the second term). The radiation of the electric dipole results in scattering of the external field by the nanosphere. The same result applies also for the electric fields. Using Eq. (2.24) we can derive from Eqs. (2.26) the distribution of the electric field inside \mathbf{E}_{in} and outside \mathbf{E}_{out} the nanosphere:

$$\mathbf{E}_{\text{in}} = \frac{3\varepsilon_r^{\text{m}}}{\varepsilon_r + 2\varepsilon_r^{\text{m}}} \mathbf{E}_0, \quad (2.28a)$$

$$\mathbf{E}_{\text{out}} = \mathbf{E}_0 + \frac{3\mathbf{n}(\mathbf{n} \cdot \mathbf{p}) - \mathbf{p}}{4\pi\varepsilon_0\varepsilon_r^{\text{m}}} \frac{1}{r^3}, \quad (2.28b)$$

where $\mathbf{n} = \mathbf{r}/r$ is the unit vector in the direction of the point where the field is studied.

Let us consider the sinusoidally varying fields of a localized oscillating source $\mathbf{E}(\mathbf{r}, t) = \mathbf{E}(\mathbf{r}) \exp(-i\omega t)$ and $\mathbf{H}(\mathbf{r}, t) = \mathbf{H}(\mathbf{r}) \exp(-i\omega t)$. From Maxwell's equations (2.1) using a Fourier analysis of the time dependence the following expression for the dipole field can be derived [42, p. 411]:

$$\mathbf{E}(\mathbf{r}) = \frac{1}{4\pi\epsilon_0\epsilon_r^m} \left\{ k^2 (\mathbf{n} \times \mathbf{p}) \times \mathbf{n} \frac{\exp(ikr)}{r} + [3\mathbf{n}(\mathbf{n} \cdot \mathbf{p}) - \mathbf{p}] \left(\frac{1}{r^3} - \frac{ik}{r^2} \right) \exp(ikr) \right\}, \quad (2.29a)$$

$$\mathbf{H}(\mathbf{r}) = \frac{ck^2}{4\pi} (\mathbf{n} \times \mathbf{p}) \frac{\exp(ikr)}{r} \left(1 - \frac{1}{ikr} \right), \quad (2.29b)$$

where $k = 2\pi/\lambda$ is the wave number and c is the speed of light in vacuum. In the near zone of the nanoparticle, where $kr \ll 1$, the fields can be simplified into

$$\mathbf{E}(\mathbf{r}, t) = \frac{3\mathbf{n}(\mathbf{n} \cdot \mathbf{p}) - \mathbf{p}}{4\pi\epsilon_0\epsilon_r^m} \frac{1}{r^3} \exp(-i\omega t), \quad (2.30a)$$

$$\mathbf{H}(\mathbf{r}, t) = \frac{i\omega}{4\pi} (\mathbf{n} \times \mathbf{p}) \frac{1}{r^2} \exp(-i\omega t). \quad (2.30b)$$

This field is called the near field of the nanosphere and is strongly decaying with r . As we can see from the expression above, the field is not propagating and does not transport energy away from the electric dipole (Note that the term $\exp(ikr)$ is missing.). The electric field, apart from its harmonic time dependence, shows the behaviour of the electrostatic point dipole, see Eq. (2.28b).

In the opposite limit of the radiation zone, $kr \gg 1$, the fields can be approximated by

$$\mathbf{E}(\mathbf{r}, t) = \frac{1}{4\pi\epsilon_0\epsilon_r^m} k^2 (\mathbf{n} \times \mathbf{p}) \times \mathbf{n} \frac{\exp(ikr)}{r} \exp(-i\omega t), \quad (2.31a)$$

$$\mathbf{H}(\mathbf{r}, t) = \frac{ck^2}{4\pi} (\mathbf{n} \times \mathbf{p}) \frac{\exp(ikr)}{r} \exp(-i\omega t). \quad (2.31b)$$

In this case, the field is called the far field and consists of propagating spherical waves because of the term $\exp[i(kr - \omega t)]$ and decays slower than the near field, with a rate of $1/r$.

We can rewrite Eq. (2.27) by introducing the polarizability α into the expression

$$\mathbf{p} = \epsilon_0\epsilon_r^m \alpha \mathbf{E}_0, \quad (2.32)$$

therefore the polarizability has the following form:

$$\alpha = 4\pi a^3 \frac{\epsilon_r - \epsilon_r^m}{\epsilon_r + 2\epsilon_r^m}. \quad (2.33)$$

The polarizability is the matter ability to polarize and is closely related to the plasmon oscillations. When the polarizability reaches the maximum value, localized

surface plasmons (LSPs) are generated in the nanoparticle. The polarizability is in a resonant state under the condition that $|\varepsilon_r + 2\varepsilon_r^m|$ is minimal. If we consider small or slowly varying $\text{Im}\{\varepsilon_r\}$, the condition is fulfilled with

$$\text{Re}\{\varepsilon_r\} = -2\varepsilon_r^m, \quad (2.34)$$

the so called Fröhlich condition.

Scattering and absorption efficiencies of the nanoparticle are characterized by cross sections C_{sca} and C_{abs} , respectively. They can be derived via the Poynting vector (Eqs. (2.15) and (2.16)) determined from Eqs. (2.29)

$$C_{\text{sca}} = \frac{k^4}{6\pi} |\alpha|^2 = \frac{8\pi}{3} k^4 a^6 \left| \frac{\varepsilon_r - \varepsilon_r^m}{\varepsilon_r + 2\varepsilon_r^m} \right|^2, \quad (2.35a)$$

$$C_{\text{abs}} = k \text{Im}\{\alpha\} = 4\pi k a^3 \text{Im} \left[\frac{\varepsilon_r - \varepsilon_r^m}{\varepsilon_r + 2\varepsilon_r^m} \right]. \quad (2.35b)$$

The cross sections are strongly enhanced at the plasmon resonance given by the polarizability of the nanoparticle and are dependent on the particle dimensions. The extinction cross section is described by

$$C_{\text{ext}} = C_{\text{sca}} + C_{\text{abs}} = 9k\varepsilon_m^{3/2} V \frac{\text{Im}\{\varepsilon_r\}}{[\text{Re}\{\varepsilon_r\} + 2\varepsilon_r^m]^2 + \text{Im}\{\varepsilon_r\}^2}. \quad (2.36)$$

2.3.2 Mie theory

We have shown through the calculations in section 2.3.1 that particles with dimensions much smaller than the wavelength of the incident light can be considered as the electric point dipoles absorbing and scattering the incident electromagnetic wave. As the size of the particle increases, the field retardation begins to play a major role, the particle is no longer polarized by the incident electromagnetic wave homogeneously and thus the quasi-static approximation cannot be applied.

The exact solution of the optical response of particles with dimensions comparable to the wavelength was published by G. Mie in 1908 [4]. However this description of the optical characteristics is available only for spheres and ellipsoids. The Mie theory is derived from the vectorial Helmholtz equation (2.7) in the spherical coordinates. This problem is transferred into solving the scalar wave equation and via scalar solution we can express the primary vectorial spherical harmonic functions. The final solution has the form of infinite series consisting of the spherical Bessel functions. A complete derivation of the scattering and absorption of electromagnetic radiation by a sphere is presented for example in [40, p. 83], here we show only main steps and the solutions.

The dependent general solutions of the vectorial Helmholtz equation (2.7) are of the form

$$\mathbf{M} = \nabla \times (\mathbf{r}\psi), \quad (2.37a)$$

$$\mathbf{N} = \frac{\nabla \times \mathbf{M}}{k}, \quad (2.37b)$$

where $\psi = \psi(r, \theta, \varphi)$ is the generating scalar function in the spherical coordinates that satisfies the scalar wave equation

$$\nabla^2 \psi + k^2 \psi = 0. \quad (2.38)$$

The solution of Eq. (2.38) is the product of three independent function

$$\psi(r, \theta, \varphi) = R(r) \Theta(\theta) \Phi(\varphi). \quad (2.39)$$

Solving Eq. (2.38) we obtain three independent equations, each for one coordinate. Two linearly independent solutions for the function Φ are

$$\Phi_e = \cos(m\varphi), \quad (2.40a)$$

$$\Phi_o = \sin(m\varphi), \quad (2.40b)$$

where m and n are the separation constants and the indices e and o denote even and odd solutions. The expression for the ψ dependence on the angle θ has the form of the Legendre functions of the first kind $P_n^m(\cos\theta)$ of degree n and order m , where $n = m, m+1, \dots$. The dependence on r is given by the Bessel functions of the first J_ν and the second Y_ν kind, where the order $\nu = n + 1/2$. The solution is any linear combination of the linearly independent spherical Bessel functions

$$j_n(\rho) = \sqrt{\frac{\pi}{2\rho}} J_{n+1/2}(\rho), \quad (2.41a)$$

$$y_n(\rho) = \sqrt{\frac{\pi}{2\rho}} Y_{n+1/2}(\rho), \quad (2.41b)$$

where we introduced the dimensionless variable $\rho = kr$.

Then we can write the general solution of the scalar wave equation (2.38):

$$\psi_{emn} = \cos(m\varphi) P_n^m(\cos\theta) z_n(kr), \quad (2.42a)$$

$$\psi_{omn} = \sin(m\varphi) P_n^m(\cos\theta) z_n(kr), \quad (2.42b)$$

where z_n is the linear combination of Eqs. (2.41). If we put the solutions given by Eqs. (2.42) in Eqs. (2.37), we obtain the vectorial spherical harmonic functions for the even modes:

$$\mathbf{M}_{emn} = \nabla \times (\mathbf{r}\psi_{emn}), \quad (2.43a)$$

$$\mathbf{N}_{emn} = \frac{\nabla \times \mathbf{M}_{emn}}{k}, \quad (2.43b)$$

and analogously for the odd modes.

In the next steps, we deal with the electromagnetic wave illuminating a spherical object, propagating in the z -axis direction and linearly polarized in the x -axis direction. The incident electromagnetic wave has to be decomposed onto the spherical harmonic waves:

$$\mathbf{E}_i = E_0 \sum_{n=1}^{\infty} i^n \frac{2n+1}{n(n+1)} \left(\mathbf{M}_{o1n}^{(1)} - i\mathbf{N}_{e1n}^{(1)} \right), \quad (2.44a)$$

$$\mathbf{H}_i = \frac{-k}{\omega\mu} E_0 \sum_{n=1}^{\infty} i^n \frac{2n+1}{n(n+1)} \left(\mathbf{M}_{e1n}^{(1)} + i\mathbf{N}_{o1n}^{(1)} \right), \quad (2.44b)$$

where k is the medium wave number and μ is the medium magnetic permeability. The field inside the sphere is

$$\mathbf{E}_1 = E_0 \sum_{n=1}^{\infty} i^n \frac{2n+1}{n(n+1)} \left(c_n \mathbf{M}_{o1n}^{(1)} - i d_n \mathbf{N}_{e1n}^{(1)} \right), \quad (2.45a)$$

$$\mathbf{H}_1 = \frac{-k_1}{\omega\mu_1} E_0 \sum_{n=1}^{\infty} i^n \frac{2n+1}{n(n+1)} \left(d_n \mathbf{M}_{e1n}^{(1)} + i c_n \mathbf{N}_{o1n}^{(1)} \right), \quad (2.45b)$$

where k_1 is the wave number inside the sphere, μ_1 is its magnetic permeability and c_n and d_n are the corresponding coefficients. The scattered field is of the following form:

$$\mathbf{E}_s = E_0 \sum_{n=1}^{\infty} i^n \frac{2n+1}{n(n+1)} \left(i a_n \mathbf{N}_{e1n}^{(3)} - b_n \mathbf{M}_{o1n}^{(3)} \right), \quad (2.46a)$$

$$\mathbf{H}_s = \frac{k}{\omega\mu} E_0 \sum_{n=1}^{\infty} i^n \frac{2n+1}{n(n+1)} \left(i b_n \mathbf{N}_{o1n}^{(3)} + a_n \mathbf{M}_{e1n}^{(3)} \right), \quad (2.46b)$$

where a_n and b_n are the corresponding coefficients. The indices (1) and (3) indicates the form of the $R(r)$ solution, $j_n(\rho)$ and the spherical Hankel function $h_n^{(1)} = j_n(\rho) + iy_n(\rho)$, respectively. Because of the boundary conditions and the orthogonality of the vectors, the coefficients for $m \neq 1$ are equal to zero. Therefore we consider only expansions for $m = 1$.

The coefficients a_n , b_n , c_n and d_n can be defined from the boundary conditions:

$$a_n = \frac{\mu m^2 j_n(mx) [x j_n(x)]' - \mu_1 j_n(x) [m x j_n(mx)]'}{\mu m^2 j_n(mx) [x h_n^{(1)}(x)]' - \mu_1 h_n^{(1)}(x) [m x j_n(mx)]'}, \quad (2.47a)$$

$$b_n = \frac{\mu_1 j_n(mx) [x j_n(x)]' - \mu j_n(x) [m x j_n(mx)]'}{\mu_1 j_n(mx) [x h_n^{(1)}(x)]' - \mu h_n^{(1)}(x) [m x j_n(mx)]'}, \quad (2.47b)$$

$$c_n = \frac{\mu_1 j_n(x) [x h_n^{(1)}(x)]' - \mu_1 h_n^{(1)}(x) [x j_n(x)]'}{\mu_1 j_n(mx) [x h_n^{(1)}(x)]' - \mu h_n^{(1)}(x) [m x j_n(mx)]'}, \quad (2.47c)$$

$$d_n = \frac{\mu_1 m j_n(x) [x h_n^{(1)}(x)]' - \mu_1 m h_n^{(1)}(x) [x j_n(x)]'}{\mu m^2 j_n(mx) [x h_n^{(1)}(x)]' - \mu_1 h_n^{(1)}(x) [m x j_n(mx)]'}, \quad (2.47d)$$

where the prime indicates the differentiation with respect to the argument in parentheses, $x = ka$ is the size parameter and m is the relative refractive index

$$m = \sqrt{\varepsilon_r} / \sqrt{\varepsilon_r^m}. \quad (2.48)$$

Using the coefficients given by Eqs. (2.47) we can describe the scattering and extinction cross sections C_{sca} and C_{ext} , respectively:

$$C_{\text{sca}} = \frac{2\pi}{k^2} \sum_{n=1}^{\infty} (2n+1) (|a_n|^2 + |b_n|^2), \quad (2.49a)$$

$$C_{\text{ext}} = \frac{2\pi}{k^2} \sum_{n=1}^{\infty} (2n+1) \text{Re}\{a_n + b_n\}. \quad (2.49b)$$

Then the absorption cross section can be simply expressed by the relationship

$$C_{\text{abs}} = C_{\text{ext}} - C_{\text{sca}}. \quad (2.50)$$

2.3.3 Discrete dipole approximation

The accurate theoretical description of cross sections can be obtained only for particles of spherical and ellipsoidal shapes (see the previous section 2.3.2). The analytical model of the scattered field can be applied also on nanorods, but only for certain parameters ($R \ll l$ and $R \ll \lambda$, where R is the radius of the nanorod, l is its length and λ is the wavelength of the incident light) [47]. However in these days, most of investigated particles have different shapes from spherical or ellipsoidal ones or nanorods do not satisfy the conditions mentioned above. Therefore to characterize optical properties of plasmonic particles with different geometries we have to use numerical calculations. These include the Finite-difference time-domain

technique (FDTD) [48] or the Discrete dipole approximation (DDA) [49]. Within this thesis we utilized the latter method because the DDA can be much faster than FDTD [50] and is available at the Institute of Scientific Instruments of the CAS where the thesis was done.

The DDA (sometimes called the Coupled dipole approximation) was proposed by Purcell and Pennypacker in 1973 [51]. The scatterer is divided into small discrete subvolumes where each of them can be replaced by a point dipole (see section 2.3.1). The external electromagnetic field induces dipole moments in each element and these point dipoles interact with each other and the external field. The dipole polarization of the whole system can be expressed by a system of linear equations. The desired cross sections of the object or other scattering properties can be obtained from the solution of the equation system.

The DDA software used for the thesis applied the CGS system, therefore the formulations in this section are held in this way. The general integral equation solved by the DDA is the following [52]:

$$\begin{aligned} \mathbf{E}(\mathbf{r}) = & \mathbf{E}^{\text{inc}}(\mathbf{r}) + \int_{V \setminus V_0} d^3r' \bar{G}(\mathbf{r}, \mathbf{r}') \chi(\mathbf{r}') \mathbf{E}(\mathbf{r}') + \mathbf{M}(V_0, \mathbf{r}) \\ & - \bar{L}(\partial V_0, \mathbf{r}) \chi(\mathbf{r}) \mathbf{E}(\mathbf{r}), \end{aligned} \quad (2.51)$$

where $\mathbf{E}(\mathbf{r})$ is the total electric field inside the scatterer at location \mathbf{r} , $\mathbf{E}^{\text{inc}}(\mathbf{r})$ is the incident electric field, $\bar{G}(\mathbf{r}, \mathbf{r}')$ is the free-space dyadic Green's function, $\chi(\mathbf{r})$ is the electric susceptibility of the material, V is the volume of the object and V_0 is a smaller volume such that $V_0 \subset V$ and $\mathbf{r} \in V_0 \setminus \partial V_0$. $\bar{L}(\partial V_0, \mathbf{r})$ is the so called self-term dyadic, the function defined via integral over ∂V_0 that depends on the shape of the subvolume V_0 but does not depend on the size of the element. On the other side, the function $\mathbf{M}(V_0, \mathbf{r})$ depends on the cell size and is defined via volume integral [52]:

$$\mathbf{M}(V_0, \mathbf{r}) = \int_{V_0} d^3r' (\bar{G}(\mathbf{r}, \mathbf{r}') \chi(\mathbf{r}') \mathbf{E}(\mathbf{r}') - \bar{G}^{\text{s}}(\mathbf{r}, \mathbf{r}') \chi(\mathbf{r}) \mathbf{E}(\mathbf{r})), \quad (2.52)$$

where $\bar{G}^{\text{s}}(\mathbf{r}, \mathbf{r}')$ is the static limit (the wave number $k \rightarrow 0$) of $\bar{G}(\mathbf{r}, \mathbf{r}')$.

To obtain the numerical solution of Eq. (2.51), we have to apply a division of the whole volume V of the scatterer into N smaller subvolumes V_i (dipoles), where $V_i \cap V_j = 0$ for $i \neq j$. The location of each subvolume V_i is given by its central point with the position vector \mathbf{r}_i . Using the usual approximation, we consider \mathbf{E} and χ constant inside each subvolume:

$$\mathbf{E}(\mathbf{r}) = \mathbf{E}(\mathbf{r}_i) = \mathbf{E}_i, \quad \chi(\mathbf{r}) = \chi(\mathbf{r}_i) = \chi_i \quad \text{for } \mathbf{r} \in V_i. \quad (2.53)$$

Then Eq. (2.51) can be rewritten into the form [52]

$$\begin{aligned} \mathbf{E}_i(\mathbf{r}_i) &= \mathbf{E}_i^{\text{inc}}(\mathbf{r}_i) + \sum_{j \neq i} \bar{G}_{ij}(\mathbf{r}_i, \mathbf{r}_j) V_j \chi_j(\mathbf{r}_j) \mathbf{E}_j \\ &+ (\bar{M}_i(V_i, \mathbf{r}_i) - \bar{L}_i(\partial V_i, \mathbf{r}_i)) \chi_i(\mathbf{r}_i) \mathbf{E}_i. \end{aligned} \quad (2.54)$$

The simplest formula of the problem can be expressed by introducing the dipole polarization \mathbf{P}_i [53]

$$\bar{\alpha}_i^{-1} \mathbf{P}_i - \sum_{j \neq i} \bar{G}_{ij} \mathbf{P}_j = \mathbf{E}_i^{\text{inc}}, \quad (2.55)$$

where $\bar{\alpha}_i$ is the dipole polarizability defined through the following relation:

$$\mathbf{P}_i = \bar{\alpha}_i \mathbf{E}_i^{\text{exc}} = V_i \chi_i \mathbf{E}_i, \quad (2.56)$$

where $\mathbf{E}_i^{\text{exc}}$ stands for the exciting electric field that is a sum of $\mathbf{E}_i^{\text{inc}}$. The polarizability is often given by the Clausius–Mossotti relation [53]

$$\alpha_i = d^3 \frac{3 \varepsilon_i - 1}{4\pi \varepsilon_i + 2}, \quad (2.57)$$

where d is the size of one dipole and ε_i is the relative permittivity at the point with the position vector \mathbf{r}_i . Note that Eq. (2.57) shows the same functional form as the function of the polarizability derived by the quasi-static approximation in section 2.3.1 (Eq. (2.33)).

From the solution of the central equation, we can obtain desired scattering quantities. The scattering amplitude \mathbf{F} for the scattering direction \mathbf{n} is [53]

$$\mathbf{F}(\mathbf{n}) = -ik^3 (\bar{I} - \hat{n}\hat{n}) \sum_i \mathbf{P}_i \exp(-ik\mathbf{r}_i \cdot \mathbf{n}), \quad (2.58)$$

where \bar{I} is the identity tensor and $\hat{n}\hat{n}$ is a tensor defined as $\hat{n}\hat{n}_{\mu\nu} = n_\mu n_\nu$. The scattering cross section C_{sca} is then given by [53]

$$C_{\text{sca}} = \frac{1}{k^2} \oint d\Omega |\mathbf{F}(\mathbf{n})|^2 \quad (2.59)$$

and the extinction and absorption cross sections are determined from \mathbf{P}_i

$$C_{\text{ext}} = 4\pi k \sum_i \text{Im}\{\mathbf{P}_i \cdot \mathbf{E}_i^{\text{inc}*}\}, \quad (2.60a)$$

$$C_{\text{abs}} = 4\pi k \sum_i [\text{Im}\{\mathbf{P}_i \cdot \mathbf{E}_i^{\text{exc}*}\} - (2/3) k^3 |\mathbf{P}_i|^2], \quad (2.60b)$$

where * denotes complex conjugation.

There are several open-source codes that utilize the DDA to compute scattering characteristics of particles of arbitrary shapes, for example DDSCAT [54], OpenDDA

[55], DDA-SI toolbox [56] and ADDA [57]. In this thesis, the DDA is implemented by the freely available program ADDA (originally “Amsterdam DDA”). ADDA is a C implementation of the discrete dipole approximation developed by A. G. Hoekstra et al. since 1994 [57]. The code has been further improved by M. A. Yurkin and coworkers [58]. ADDA has a versatile spectrum of applications and its biggest advantage is that a single ADDA simulation can run on a multiprocessor system or a multicore processor so the calculations are highly speeded up.

The ADDA manual [59] describes conditions of validity, capabilities and formulation of a scattering problem. Here we introduce the general applicability of ADDA and the fundamental characterization of the computational problem. The crucial parameter is a dipole size d . It has to be small compare to any structural length of the scatterer and the wavelength of the incident light λ . This condition for particles of a size comparable to the wavelength is given by the rule of thumb:

$$d = \frac{\lambda}{10|n|}, \quad (2.61)$$

where $n = \sqrt{\epsilon_r}$ is the refractive index of the scatterer. The refractive index should be in the interval

$$|n - 1| < 2. \quad (2.62)$$

If the Eq. (2.62) is not satisfied, it can be compensated by the rapid increase of the number of dipoles in the system. For smaller scatterers (nanoparticles), the condition for d expressed by Eq. (2.61) is not satisfactory. The shape of the particle should be adequately described by dipoles so it is recommended to apply at least ten dipoles for the smallest dimension.

The fundamental ADDA code is written for particles in vacuum. To count a particle in a homogeneous non-absorbing dielectric medium with the refractive index n^m , the refractive index of the scatterer has to be replaced by the relative index n/n^m and the wavelength by the wavelength in the medium λ/n^m .

The program contains several predefined shapes of scatterers with definable parameters, for example sphere, ellipsoid, line, plate, cylinder and other. Other shapes have been still implemented but it is also possible to create a new shape through C language. The orientation of the scatterer is determined by three Euler angles, using the so called “*zyz* notation”. The direction, the polarization and the type of the incident beam can be specified, too. Its direction is given by the certain propagation vector and its type can be the ideal plane wave or an approximate description of a Gaussian beam.

The parameters mentioned above are the fundamental characters of the ADDA simulations, but of course the whole system is much more complex problem. More detailed information can be found in the documentation of the code [59].

2.3.4 Size and shape effects

Bulk dielectric functions derived from the Drude theory even with Lorentzian terms (see section 2.2) cannot be simply applied to the small particles without modifications. A dielectric function is dependent on a size and a shape of the small particle because for example the electron mean free path can be limited by the particle proportions. Another effect originating from the higher surface-to-volume ratio comes from the so called surface electronic states. Those states can be easily omitted in bulk, but have a nonnegligible effect in nanoparticles.

The approximation for the condition of the resonance behaviour derived through the Mie theory using the higher term of the expansion indicates the size dependence of the dielectric function and consequently the resonant frequency [40, p. 329]:

$$\varepsilon_r = - \left(2 + \frac{12}{5} x^2 \right) \varepsilon_r^m, \quad (2.63)$$

where $x = 2\pi a/\lambda$ is the size parameter with the radius a . With an increasing size parameter the resonance is red-shifted to longer wavelengths.

Except of the resonance-position shift with the increasing particle size, the resonant bandwidth is also changed. If we take into account the formula for the dielectric function using the Lorentzian terms (Eq. (2.14)), the resonant bandwidth is given by the damping constant γ . The mean free path of conduction electrons in a bulk is given by τv_F , where v_F is the bulk Fermi velocity. At room temperature, the mean free path in bulk gold is about 42 nm [39]. If the nanoparticle is of a diameter $2a$ about or below the dimension of the mean free path, we have to consider not only the damping by the scattering γ_0 with the ionic cores but also with the surface. Then the damping is given by [60]

$$\gamma = \gamma_0 + \frac{v_F}{a}. \quad (2.64)$$

Thus the dielectric function is not dependent only on the material and the frequency of the incident field but also on dimensions of the particle. Optical properties for a gold particle are shown in Tab. 2.1. For small nanoparticles the scattering time decreases rapidly while decreasing the dimensions which means an increase in the damping γ and therefore the broadening of the scattering peak.

On the other hand, if the dimensions of the nanoparticle are larger (for a gold particle in an aqueous solution with $2a > 25$ nm [8]), the retardation effects are more significant and the bandwidth is broadened with increasing dimensions [14]. This dependence of the bandwidth on the particle diameter is shown in Fig. 2.3.

To describe the resonant modes in arbitrarily shaped scatterers, it desires more effort and the analytic solution is often unknown. Spheroids and ellipsoids can be treated in the similar way as spheres and resonant modes in infinite cylinders can be

Tab. 2.1: Optical properties (the scattering time τ and the dielectric function ε_r) for gold particles of a different radius a at the wavelength of 500 nm [39, 61].

	$\tau / 10^{-15} \text{ s}^{-1}$	ε_r
bulk	24.7	$-2.68 - 3.09i$
$a = 100 \text{ nm}$	14.6	$-2.68 - 3.19i$
$a = 10 \text{ nm}$	3.1	$-2.59 - 4.08i$

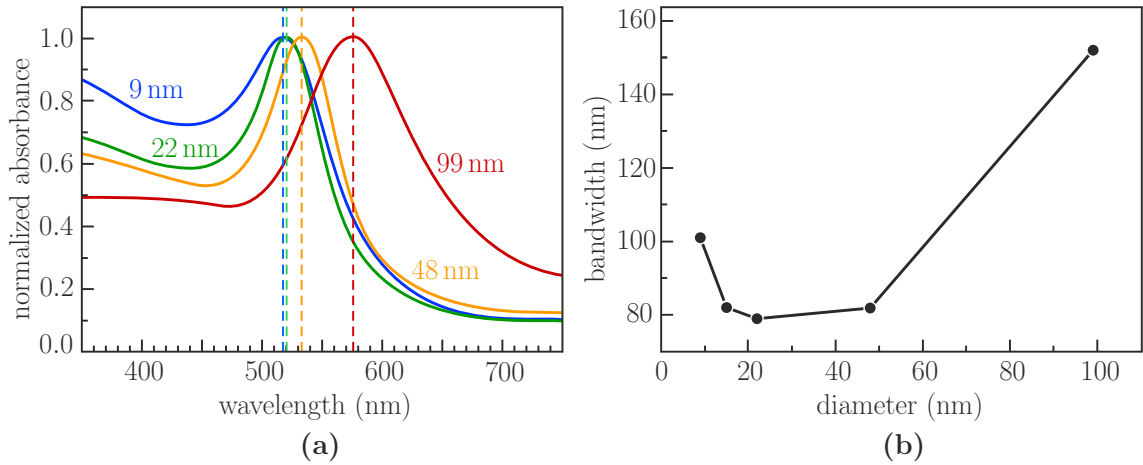


Fig. 2.3: (a) Normalized absorption spectra of colloidal aqueous solutions of spherical gold nanoparticles with diameters of 9 nm, 22 nm, 48 nm and 99 nm; (b) The plasmon bandwidth as a function of a particle diameter; taken from [62], originally from [8].

defined analytically, too [40, p. 342]. The exact theory for particles with more complex shapes is quite complicated and these problems are usually solved numerically.

The model example of the LSP resonance in a particle with a shape different from a sphere is a nanorod. From the geometrical insight we see that there are two major directions of the electron oscillations in the nanoparticle, namely the one where the electrons oscillate along the rod axis (the longitudinal mode – LM) and the second one, electronic oscillations perpendicular to the rod axis (the transversal mode – TM), see Fig. 2.4a. The restoring force proportional to the charge accumulation is larger in the TM and hence, the resonant frequencies are higher and the resonant wavelengths shorter in this mode [60]. In longer nanorods, the resonant wavelength of the LM is shifted to longer wavelengths. The dependence of the resonant wavelengths of LMs and TMs in nanorods with different aspect ratios a/b is depicted in Fig. 2.4b. The LSP resonance is easily tunable by changing the dimensional parameters of nanoparticles and therefore, these particles can be used for biosensing [29] or optoelectronics [30].

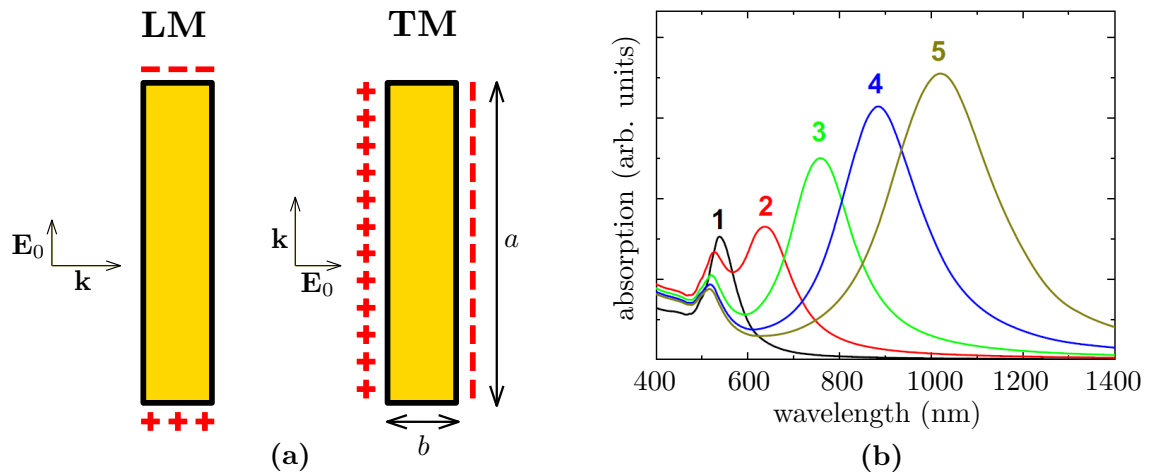


Fig. 2.4: (a) Scheme of a charge accumulation for longitudinal (LM) and transversal (TM) modes in a nanorod; adapted from [60]; (b) Calculated absorption spectra for gold nanorods with different aspect ratios $a/b = 1-5$ indicated in the figure, the peak in shorter wavelengths represents the TM and in longer wavelengths is a peak for the LM (for a higher aspect ratio it is evident its red shift to longer wavelengths); taken from [60].

Using the linearly polarized light for illumination of a plasmonic particle, these two modes can be excited separately. Nevertheless all particles in a solution should be oriented in the same way or the optical spectra should be taken only from one nanoparticle with a defined orientation. This requirement can be achieved by using the optical tweezers (described in section 3.1.1), where the object of interest is op-

tically trapped and can be aligned by changing the direction of the trapping-laser polarization [16]. An example of such a behaviour is illustrated in Fig. 2.5a. The scattering spectra of an elongated silver nanoparticle were obtained using two different polarization directions of the illumination. Blue points represent the transversal mode and green points stand for the longitudinal mode.

In an optical trap, more nanoparticles might be held together. The number of trapped particles can be determined through scattering intensities which are linearly proportional to the number of nanoparticles in the optical trap [63]. If the optical trap contains more nanoparticles (approximately ten nanoparticles), the scattering spectrum is slightly red-shifted and broader due to the interparticle coupling because trapped particles are more close to each other, see Fig. 2.5b.

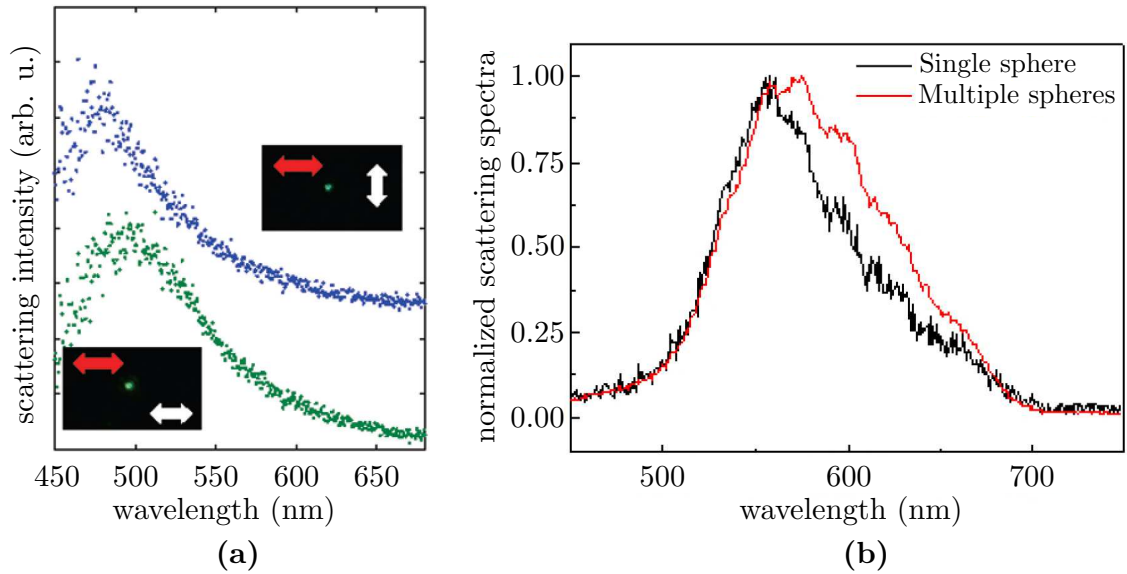


Fig. 2.5: (a) Dark-field images and scattering spectra of an elongated silver nanoparticle in an aqueous solution in an optical trap. The scattering spectrum is red-shifted for the polarization direction of illumination (white arrows) parallel to the trapping-laser polarization direction (red arrows); taken from [16]; (b) Normalized scattering spectra of trapped single and multiple gold nanoparticles with a diameter of 50 nm in an aqueous solution. The spectrum for multiple particles is red-shifted and broader due to the interparticle coupling; taken from [63].

3 SPECTROSCOPY OF OPTICALLY TRAPPED PARTICLES

Within this thesis, we deal with an optical response of a single isolated nanoparticle or nanoparticle clusters in an aqueous solution. For their applications, there is clear demand for their optimized LSP characteristics; for example nanoparticle LSP modes are sensitive to any change in the surrounding refractive index and one can exploit the resulting resonance-wavelength shift for biosensing. Knowing and tuning the LSP resonance allow us to enhance the sensitivity of these biosensors. A straightforward technique used within this work for the investigation of an optical response is the optical trapping and the optical spectroscopy of particles in an aqueous solution. This method allows us to select particles from a colloidal solution and record their scattering spectra for the desired time.

At the beginning of this chapter we explain principles of the optical trapping and the dark-field spectroscopy and show a schematic diagram of an experimental setup. Then we deal with a characterization of the particle scattering. At first we test the optical setup with polystyrene particles and show the dependence of the scattering intensity on the illumination alignment and the trapped-particle count. Then we focus on the field scattered by metallic nanoparticles, silver and gold. We show obtained experimental data and also theoretical calculations of scattering cross sections.

3.1 Experimental techniques

In order to have a possibility to characterize just a single metallic nanoparticle or a desired number of them, we used the optical tweezers combined with a dark-field spectroscopy. It allowed us to select a nanoparticle from a colloidal solution and manipulate it at will. Individual nanoparticles could be seen as bright spots in a camera and their scattering spectra were recorded by a spectrometer.

3.1.1 Optical trapping

For trapping and precise manipulation of nanoparticles or microobjects, it is possible to use a light beam. The first studies on optical forces acting on an object were performed by A. Ashkin in 1970 [64], when he demonstrated microobject levitation in light. In 1978, he proposed an idea about the optical trapping of atoms by a highly focused laser beam [65] and later he published an article about the optical trapping of dielectric particles [66].

We distinguish two main types of optical forces that act on a dielectric particle trapped by optical tweezers, radiation pressure force and gradient force. The radiation pressure force can be easily estimated from a corpuscular nature of light. A magnitude of a photon momentum p_{photon} is given by

$$p_{\text{photon}} = \frac{h\nu n^{\text{m}}}{c}, \quad (3.1)$$

where h is the Planck constant, $\nu = \omega/2\pi$ is the frequency of the electromagnetic wave and n^{m} is the refractive index of a medium. Let us consider an electromagnetic wave illuminating a cube with a wall oriented perpendicular to a trapping-laser beam. Some photons can be absorbed, then the change of their momentum magnitude is

$$\Delta p_{\text{photon}} = -\frac{h\nu n^{\text{m}}}{c}, \quad (3.2)$$

where some of them are reflected with the change of their momentum magnitude two times larger compared to the absorbed one. The number of absorbed and reflected photons is given by the material reflectance R .

The average force F_{photon} acting on a single photon is connected with its momentum change through the second Newton's law of motion [67]

$$F_{\text{photon}} = \frac{\Delta p_{\text{photon}}}{\Delta t}, \quad (3.3)$$

where Δt is the time segment. According to the third Newton's law of motion, the average force F_{object} acting on an object can be expressed through the force F_{photon} , its direction is opposite and its size is given by the number of photons N and the reflectance R [67]:

$$\begin{aligned} F_{\text{object}} &= -N(1+R)F_{\text{photon}} = -N(1+R)\frac{\Delta p_{\text{photon}}}{\Delta t} = -N(1+R)\frac{-h\nu n^{\text{m}}}{c\Delta t} \\ &= P\frac{n^{\text{m}}(1+R)}{c}, \end{aligned} \quad (3.4)$$

where $P = Nh\nu/\Delta t$ is the power of the incident light.

If a particle placed in a single-beam gradient laser trap is much larger than the wavelength of the trapping light, the gradient force can be demonstrated through the ray optics model using the momentum transfer [67]. When the light illuminates a particle, except of the reflection and the absorption of the incident light some part of the light is refracted. This process is schematically shown in Fig. 3.1. The momentum of the incident light is \mathbf{p}_i and the momentum of the refracted light is \mathbf{p}_r . Then the change of the photon momentum is $\Delta\mathbf{p} = \mathbf{p}_r - \mathbf{p}_i$. As described above, the force from one photon acting on an object can be obtained through the Newton's laws of motion from the change of the photon momentum:

$$\mathbf{F}_{\text{object}} = -\mathbf{F}_{\text{photon}} = -\Delta\mathbf{p}/\Delta t. \quad (3.5)$$

If we summarize all photons acting on an object situated on the axis of the diverging beam, the resultant force \mathbf{F}_{grad} acts in the axis of the incident beam and its orientation depends on the beam divergence. This force causes pushing a particle to the focus of the incident beam, thus if a particle is behind a focal point, the force is oriented oppositely to the direction of the beam propagation. If the particle is deflected from the axis of the beam, the radial forces push a particle back into the axis of the beam. Once the gradient force is in the balance with the radiation pressure force, the total force acting on the particle is equal to zero and a particle is fully trapped.

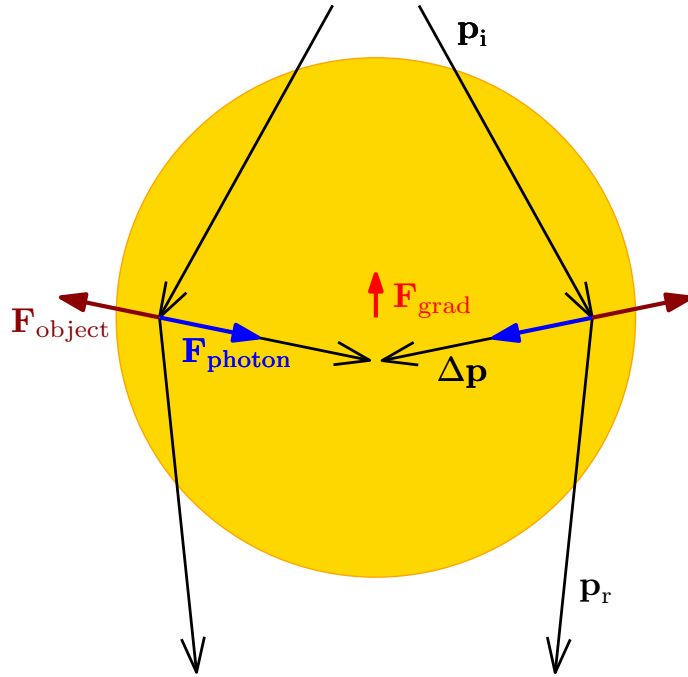


Fig. 3.1: Scheme of the ray optics model. An incident photon is refracted and the change of its momentum $\Delta\mathbf{p} = \mathbf{p}_r - \mathbf{p}_i$ causes pushing a particle to the focus of the incident beam by the gradient force $\mathbf{F}_{\text{grad}} = \sum \mathbf{F}_{\text{object}} = \sum -\mathbf{F}_{\text{photon}}$.

If the size of a particle fulfils the condition for the quasi-static approximation described in section 2.3.1 ($a \ll \lambda$), the optical force acting on a nanoparticle can be expressed analytically [39]. The total optical force \mathbf{F} is given by integrating the optical force density \mathbf{f} over the whole volume V of a particle:

$$\langle F_i \rangle = \int_V \langle f_i \rangle dV, \quad (3.6)$$

where i symbolizes one component of the vector and the brackets $\langle \dots \rangle$ correspond to the time average over the period $T = 2\pi/\omega$. There are several approaches how to calculate the optical force density [39], for example the following expression of the

Lorentz force, that applies for a nonmagnetic particle and a nonmagnetic medium:

$$\langle \mathbf{f} \rangle = \frac{1}{2} \text{Re} \left\{ (\mathbf{P} \cdot \nabla) \mathbf{E}^* + \frac{\partial \mathbf{P}}{\partial t} \times \mu_0 \mathbf{H}^* \right\}. \quad (3.7)$$

Using the relation for the induced polarization \mathbf{p} with the polarizability α (Eq. (2.32)), we arrive at the formula

$$\langle \mathbf{f} \rangle = \frac{\varepsilon_0 \varepsilon_r^m}{2} \text{Re} \left\{ \alpha (\mathbf{E} \cdot \nabla) \mathbf{E}^* + \alpha \frac{\partial \mathbf{E}}{\partial t} \times \mu_0 \mathbf{H}^* \right\}. \quad (3.8)$$

The expression of the total optical force given by this optical force density can be split into the gradient force and the scattering force. The gradient force that causes attracting a nanoparticle into the focal spot is given by

$$\langle \mathbf{F}_{\text{grad}} \rangle = \frac{\varepsilon_0 \varepsilon_r^m}{4} \text{Re} \{ \alpha \} \nabla (\mathbf{E} \cdot \mathbf{E}^*), \quad (3.9)$$

where we used the vector identity $\nabla (\mathbf{E} \cdot \mathbf{E}^*) = 2 \text{Re} \{ (\mathbf{E} \cdot \nabla) \mathbf{E}^* + \mathbf{E} \times (\nabla \times \mathbf{E}^*) \}$ and the Maxwell's equation (2.1c). From the Eq. (3.9) we can see that the gradient force depends on the gradient of the intensity of the incident electromagnetic wave. This gradient can be increased for example by using a microscope objective to focus the beam into the diffraction-limited spot. The gradient force might be even more increased by an immerse objective, where the numerical aperture exceeds the value 1.

The scattering force is connected with the momentum loss or transfer from the incident beam to a particle, as mentioned above. This force is a sum of the force due to scattering by an object $\langle \mathbf{F}_{\text{sca}} \rangle$ and the force due to particle absorption $\langle \mathbf{F}_{\text{abs}} \rangle$:

$$\langle \mathbf{F}_{\text{sca}} \rangle + \langle \mathbf{F}_{\text{abs}} \rangle = \frac{n_r^m}{c} C_{\text{sca}} \langle \mathbf{S} \rangle + \frac{n_r^m}{c} C_{\text{abs}} \langle \mathbf{S} \rangle, \quad (3.10)$$

where $\langle \mathbf{S} \rangle = 1/2 \text{Re} \{ \mathbf{E} \times \mathbf{H}^* \}$ is the time averaged Poynting vector and C_{sca} and C_{abs} are the scattering cross section and the absorption cross section, respectively, given by Eqs. (2.35).

As the size of a nanoparticle increases, these expressions presented above are no longer valid and the behaviour of the particle illuminated by the electromagnetic wave is much more complex. For the description of such a particle optical trapping, the Lorentz–Mie scattering theory is used [68]. The incident wave has to be decomposed onto the spherical harmonic waves and the whole problem is solved through the Mie theory.

Trapping of metallic nanoparticles is more complex than trapping of dielectric particles because of the plasmon oscillations. If the trapping laser is tuned close to the resonant wavelength of the nanoparticle (for silver and gold in the visible and near infrared range), the scattering force increases and thus sometimes it is

impossible to trap the particle. On the other hand, if the wavelength of the trapping laser is far from the nanoparticle resonance, the trapping of metallic nanoparticles is similar to trapping of high refractive-index dielectric nanoparticles [39].

The other limitation for the optical trapping of metallic particles is their size. Up to the size of 50 nm the scattering cross section is negligible compared to the gradient force. For larger spherical metallic particles, the scattering force begins to play a major role and the particle cannot be stably trapped. But some non-spherically shaped metallic particles of the size of 10^2 nm can be oriented in the optical trap in a stable position and can be fully trapped [10].

The efficiency of the optical trapping is characterized via the trap stiffness κ . This parameter depends on the particle size and shape, the dynamic viscosity of the medium and the corner frequency in the power spectral density [10]. The trap stiffness of the single focused beam for nanoparticles of different sizes and shapes are compared in Fig. 3.2a (lateral trap stiffness) and Fig. 3.2b (longitudinal trap stiffness). For smaller particles the trap stiffness strongly depends on the particle diameter d . The penetration depth of gold particles is about 50 nm and therefore the spherical particles of diameter $d < 100$ nm interact with the incident electromagnetic wave by their entire volume $V \propto d^3$. Larger particles interact with the incoming electromagnetic field just by a surface layer and thus the trap stiffness is proportional to the diameter square.

One can see from the graphs in Fig. 3.2 that the longitudinal trap stiffness is about one order weaker than the lateral trap stiffness. Therefore it is much more difficult to trap particles in the z direction (beam-propagation direction) than in the xy plane (the plane perpendicular to the beam propagation).

3.1.2 Köhler dark-field illumination

Within this thesis, metallic nanoparticles in a single-beam gradient laser trap were illuminated by Köhler illumination. Köhler illumination is a type of the specimen illumination that was design by A. Köhler in 1893 [69]. An image of the illumination source at the sample plane is totally defocused and thus this illumination is extremely even.

The fundamental optical components in the setup for the Köhler illumination are collector lens, field diaphragm, condenser diaphragm and condenser lens set in this order between the light source and the sample (see Fig. 3.3). In our installation, we additionally use a collimator lens placed between the collector lens and the condenser lens. In the bright-field illumination, the collector lens collects the light from the halogen lamp and with help of the collimator lens the image of the light source is formed at the plane of the condenser diaphragm. The second set of conjugate image

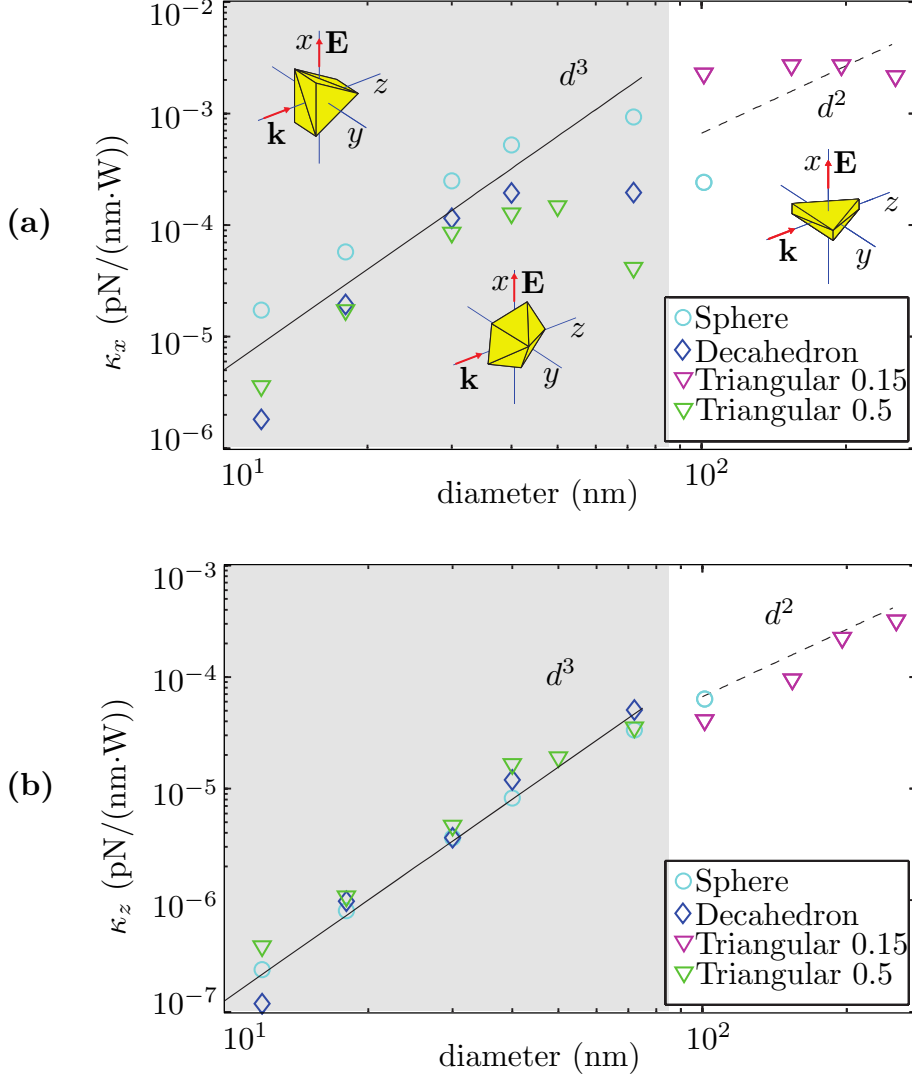


Fig. 3.2: (a) Lateral (κ_x) and (b) longitudinal (κ_z) trap stiffnesses of optically trapped gold nanoparticles of different sizes and shapes (spheres, decahedrons and triangular prisms of different aspect ratios – 0.15 and 0.5) in an aqueous solution calculated by Mie theory and DDA. The wavelength of the trapping laser $\lambda = 1064$ nm, the numerical aperture $NA = 0.37$, the incident power $P = 1$ W; taken from [10].

planes is the projection of the field diaphragm whose image is formed at the sample plane.

Köhler dark-field illumination has the similar alignment of the optical components as the bright-field illumination, only the condenser diaphragm is replaced by the dark-field annulus. The field diaphragm is always fully open allowing the condenser to operate at its maximum numerical aperture. In the dark-field illumination, the light cone illuminating the sample (The central beam is blocked by the condenser diaphragm.) is not directly collected by the objective lens, only the light scattered by a sample can pass through the objective aperture (see the inserted scheme in Fig. 3.4). Then objects look like bright spots in the dark background. To provide this type of illumination, the numerical aperture of the condenser lens has to be higher than the numerical aperture of the objective.

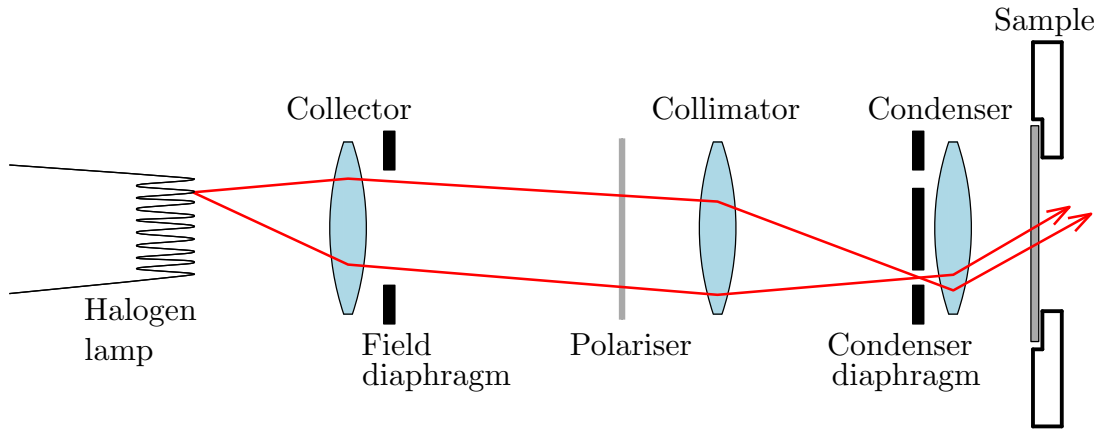


Fig. 3.3: The optical setup of Köhler dark-field illumination consisting of halogen lamp, collector lens with field diaphragm, polariser, collimator lens and condenser lens with condenser dark-field diaphragm. The red line represents the beam path, the image of the light source is formed at the condenser-diaphragm plane and is totally defocused at the sample plane.

In the setup used within this thesis, the sample illumination is provided by unpolarized white light from the 100W halogen lamp OSRAM 64627 focused into a fibre bundle. The light is collected by the aspherical lens with the focal length $f' = 20$ mm (AL2018) and collimated by the achromatic doublet with $f' = 100$ mm (AC254-100-A). The numerical aperture of the oil dark-field condenser (Olympus U-TLO) is 1.4 with the dark-field annulus of the diameter approx. 19 mm. The linear polariser is implemented into the experimental setup in order to have a possibility to choose the polarization direction of the light illuminating the sample.

3.1.3 Experimental setup

Details of the experimental setup used in this work are schematically illustrated in Fig. 3.4. In general, the optical setup has three parts: optical tweezers, Köhler dark-field illumination and a branch for a detection of the scattered light. Plasmonic nanoparticles in an aqueous solution are trapped using a single-beam gradient laser trap. The trapping laser Adlas GmbH & Co. is tuned at the wavelength of 1064 nm that is far from the expecting resonance of the examined plasmonic particles (in the visible range). The linearly polarized laser beam should slightly overfill the back aperture of the objective used for the optical trapping, therefore the beam from the laser source is expanded by a beam expander consisting of two aspherical doublets from Thorlabs with focal distances $f'_{L_1} = 40$ mm (AC254-040-C) and $f'_{L_2} = 200$ mm (AC254-200-C). Then the expanded laser beam passes through the filter in order to filter out all wavelengths generated by exciting diodes in the laser except of the trapping one (1064 nm). The filtered beam is reflected at the dichroic mirror and focused at the sample plane from below by the oil objective (Olympus PlanC N 100 \times) with the tunable numerical aperture $NA = 0.6-1.25$. A sample is fixed in a sample holder that allows a sample to be positioned manually in the 3D space with the precision of tens of micrometers.

A nanoparticle trapped by the optical tweezers is illuminated from above by the Köhler dark-field illumination, described in the previous section 3.1.2. Only the light scattered by a nanoparticle is collected with the same objective as used for the optical trapping. Then the beam passes through the dichroic mirror and is focused by the tube lens L_3 into the color camera Basler aCA2000-50gc where objects scattering the incident light can be observed. To examine scattering spectra of nanoparticles, the scattered light has to be analysed by a spectrometer. Therefore the mirror reflecting the beam into the camera (M_4) is a flip mirror that might be easily removed from the beam path. It enables the beam to pass directly into the optical fibre that is connected to the spectrometer Maya2000 Ocean Optics. This spectrometer is of the Czerny-Turner type [70] which means that the light is collimated to a grating where the light is diffracted. The diffracted light is focused at a detector plane where the information about intensities in dependence on the light wavelength from 200 nm to 1100 nm is obtained.

The detection of the scattered light is based on a confocal microscopy [71]. This technique eliminates the out-of-focus light by a spatial pinhole placed at the confocal plane of the tube lens. In our setup, the spatial pinhole is done through the spectrometer fibre with the aperture of 200 μm and thus the light is collected predominantly from the trapped nanoparticle.

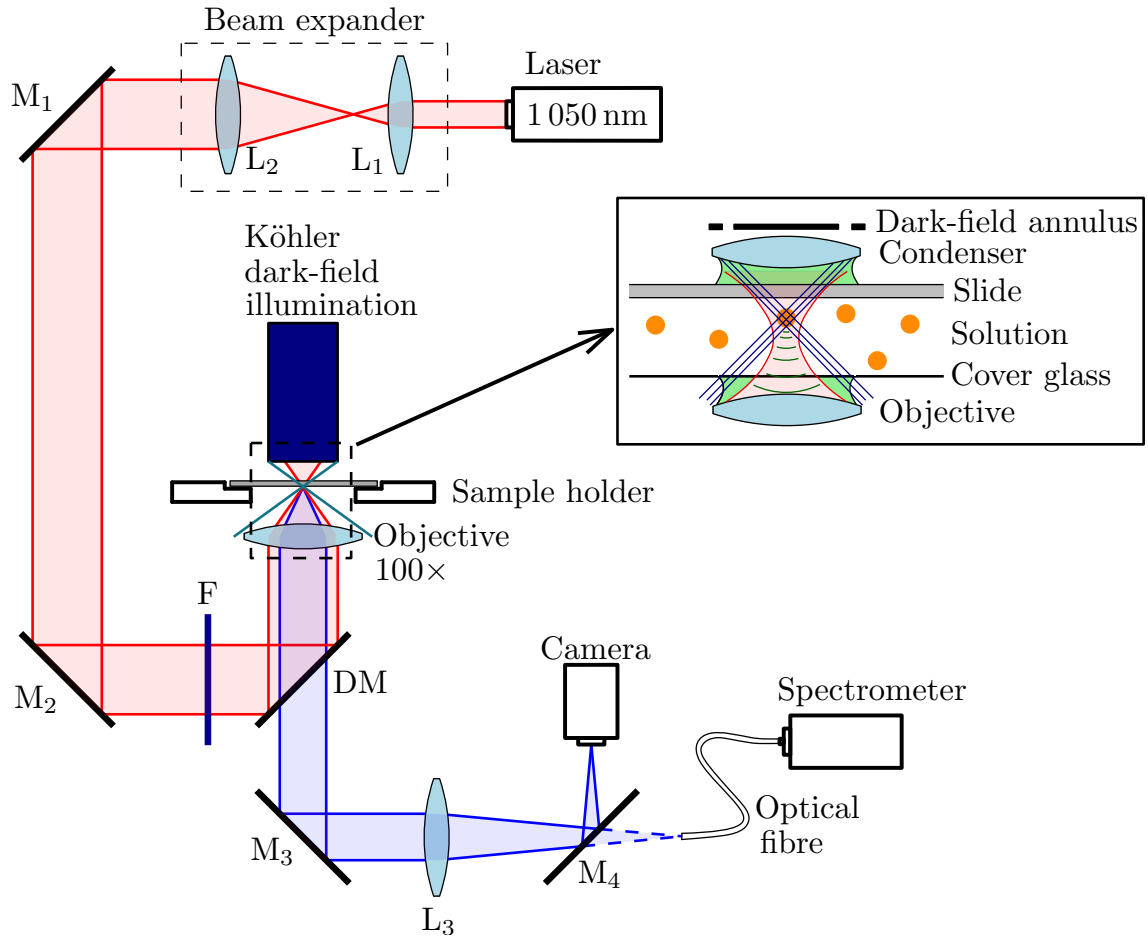


Fig. 3.4: The scheme of the setup used in this work. A nanoparticle is trapped by the optical tweezers and illuminated by the Köhler dark-field illumination. The scattered light is detected in the camera and the spectrometer. The beam path is represented by red (trapping laser) and blue (scattered light) lines. L_1 , L_2 – lenses of the beam expander; M_1 , M_2 , M_3 – dielectric mirrors; F – filter; DM – dichroic mirror; L_3 – tube lens; M_4 – flip dielectric mirror. The inserted image is the detail of the particle trapping and the dark-field illumination. The red line is the trapping beam, the blue lines represent the dark-field illumination and the green lines represent the particle scattering.

In the beam path for the optical trapping, dielectric mirrors (M_1 , M_2 , Thorlabs broadband dielectric mirrors, 750–1100 nm) suitable for the wavelength of the trapping laser are used. In the optical branch for the detection of the scattered light, we placed broadband dielectric mirrors (M_3 , M_4 , Thorlabs broadband dielectric mirrors, 350–950 nm) with the high reflectance over spectral ranges suitable for the scattered light.

The dichroic mirror in the setup is applied to reflect the laser beam into the microscope objective and has to be transparent for the scattered light. To meet this requirements, the Thorlabs mirror blanks with the surface flatness of $\lambda/10$ was coated with an one-dimensional photonic structure (2925 nm thick) where layers of titanium dioxide (120 nm thick) and silica (220 nm thick) alternate. The coating was performed by plasma ion assisted deposition by Mgr. J. Oulehla at the Institute of Scientific Instruments of the CAS. The transmittance of the dichroic mirror for s- and p-polarized light incident at the angle of 45° is plotted in Fig. 3.5. The transparent window is from 400 nm to approximately 950 nm that is suitable for the light scattered by a metallic nanoparticle. The transmittance at the trapping-beam wavelength (1064 nm) approaches the zero value, therefore the trapping-laser beam does not pass through the dichroic mirror and is mostly reflected.

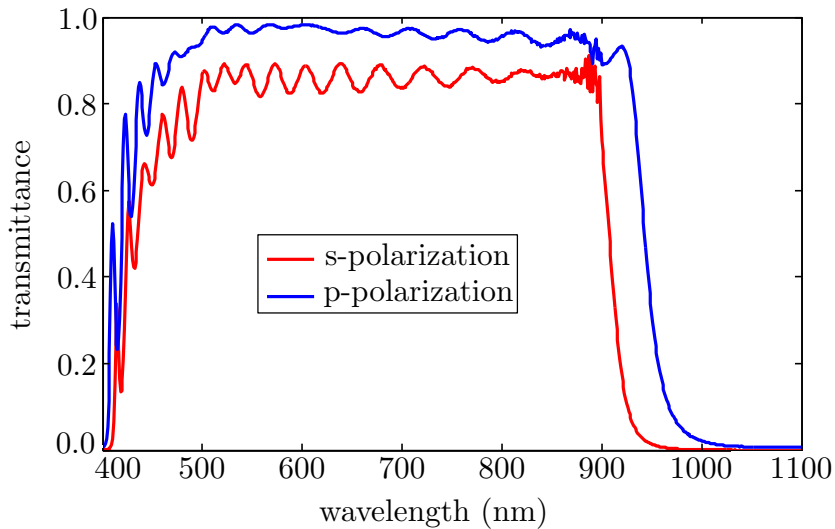


Fig. 3.5: The dependence of the transmittance of the dichroic mirror used in the setup on the wavelength of the light incident at the angle of 45° with s-polarization (red curve) and p-polarization (blue curve). The transparent window is in the range of the visible light which is mostly in accord with the light scattered by metallic nanoparticles.

Using the experimental setup with the optical components described above, the spectrum of the halogen lamp with spectral variations in the system response (hereinafter illumination spectrum and consequently illumination intensity) was recorded by the spectrometer (see Fig. 3.6). A testing sample was the demineralized water that was later applied also in aqueous colloidal solutions. The integration time for one spectrum was 7 ms and this final spectrum was obtained by averaging 500 spectra and the consequential background subtraction. If we compare the transmittance of the dichroic mirror plotted in Fig. 3.5 with the illumination spectrum in Fig. 3.6, it is apparent that the illumination spectrum is partially influenced by the dichroic mirror. But the spectrum of the halogen lamp itself plays a main role. The illumination intensity starts to increase at the wavelength $\lambda = 400$ nm and is approximately zero for wavelengths longer than $\lambda = 900$ nm. Thus the examined nanoparticles have to fulfil the resonance condition for wavelengths in this transparent window. The illumination intensity in the transparent window is oscillating therefore it is necessary to take into account the profile of the illumination spectrum and scattering spectra of nanoparticles have to be corrected for spectral variations in system response.

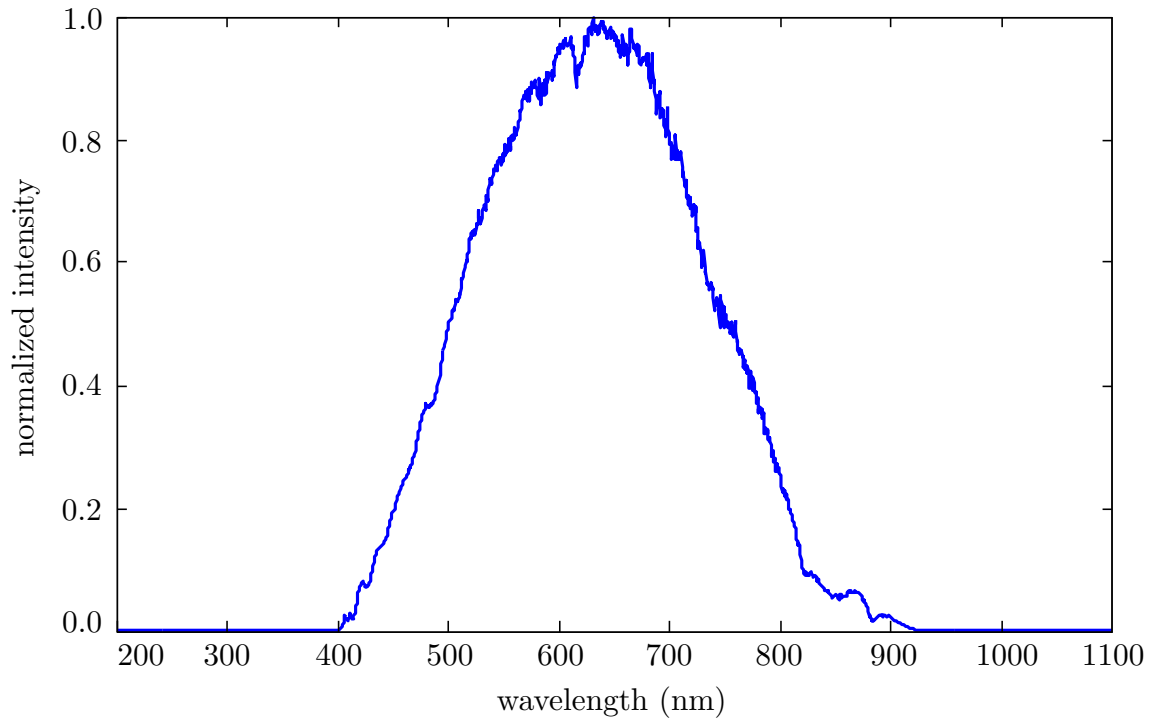


Fig. 3.6: The normalized spectrum of the halogen lamp with spectral variations in the system response recorded through a sample with the demineralized water.

3.2 Characterization of nanoparticle scattering

In this section, we present experimental results that we achieved in the field of a nanoparticle scattering. Examined particles are trapped by the optical tweezers and illuminated by the Köhler dark-field illumination, described in the previous section. Since the requirements for the numerical aperture of the objective for the optical trapping and the dark-field imaging are contradictory, it is a big deal to align the whole setup for the efficient signal collection of the trapped particle. We describe the scattering of polystyrene particles that were used for the alignment purpose. We show the scattering-intensity dependence on the number of trapped particles and the illumination alignment. Then we focus on the trapping and the optical characterization of silver nanoparticles. At the end of this section we give a comment on problems of the optical trapping and the optical spectroscopy of gold nanoparticles.

3.2.1 Setup alignment using polystyrene particles

At first we tested the experimental setup to assure the proper optical alignment. For that purpose we used a colloidal solution of spherical polystyrene particles with a diameter of 400 ± 5 nm (Thermo Scientific – Duke Standards [72]). The solution was suitably diluted by the filtered demineralized water in order to allow us to trap a single particle but the density of the solution should also allow us to find other particles in an acceptable time. 50 μ l of the prepared solution was applied on the 1mm thick slide with the 0.1mm thick spacer. The slide with the solution was covered by the cover glass with a thickness of 0.17 mm. The edges of the cover glass were closed by a transparent nail polish to prevent the sample from its drying and the liquid flow.

Then a drop of the immersion oil of the type B (the refractive index $n_D = 1.5150 \pm 0.0002$ and the Abbe number $V_D = 42.6$) was applied on the objective and the condenser lens and the prepared sample was inserted in between these two lenses. The position of the settings for the bright-field illumination had to be aligned in the way that the illumination was centred with the trapping laser beam and the image of the field diaphragm was formed at the sample plane. Because of the chromatic aberration and the diffraction on the aperture of the half-closed field diaphragm, the illumination position for the field-diaphragm image differs for different illumination wavelength. In Fig. 3.7, images of the field diaphragm in different positions of the illumination setup are shown. All colours from the illumination spectrum appears during the illumination-settings moving. It signifies that scattering spectra of examined particles could be strongly dependent on the alignment of

the optical components even for the fully opened field diaphragm. The polystyrene particles could be clearly observed in the bright field and the contrast could be even more enhanced by half-closing of the field diaphragm (see Fig. 3.8a).

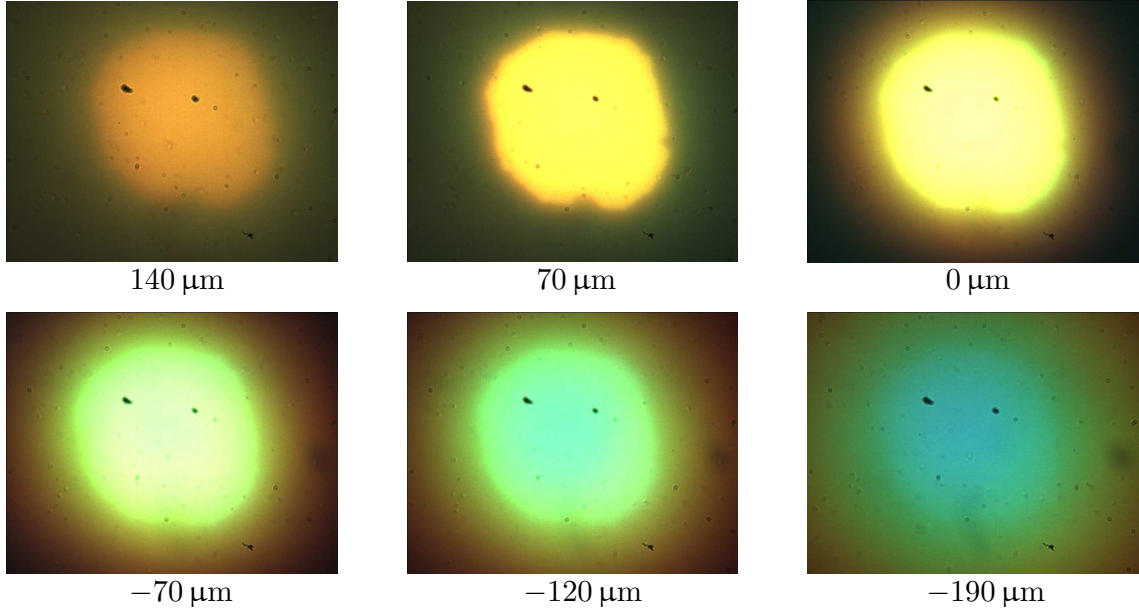


Fig. 3.7: Images of the field diaphragm in different distances of the illumination settings from the sample plane. The positions of the illumination settings are relative to the illumination position that was used for the bright-field imaging.

Afterwards we aligned the setup for the dark-field illumination. The condenser diaphragm was changed into the dark-field annulus and the whole illumination settings was moved to obtain as high scattering signal as possible. The numerical aperture of the objective had to be in balance with the numerical aperture of the condenser lens. The higher numerical aperture of the objective is necessary for the effective optical trapping but for the dark-field illumination the objective numerical aperture should be lower than the condenser numerical aperture. The dark-field image of the polystyrene solution is shown in Fig. 3.8b. The polystyrene particles appear like discoloured points in dependence on the distance from the illumination. The particle colours are analogous to the images of the field diaphragm with the different illumination positions in Fig. 3.7. The chromatic aberration of the system and the diffraction on the annulus are significant.

We trapped a single polystyrene particle and observed this change in the scattering spectra in dependence on the illumination distance from the sample plane (Fig. 3.9). The trapping-laser power was approximately 40 mW in front of the filter, and the transmission of the objective is about 40%. Each spectrum was recorded for 8 s. The final spectrum was obtained by averaging 10 measurements of the same

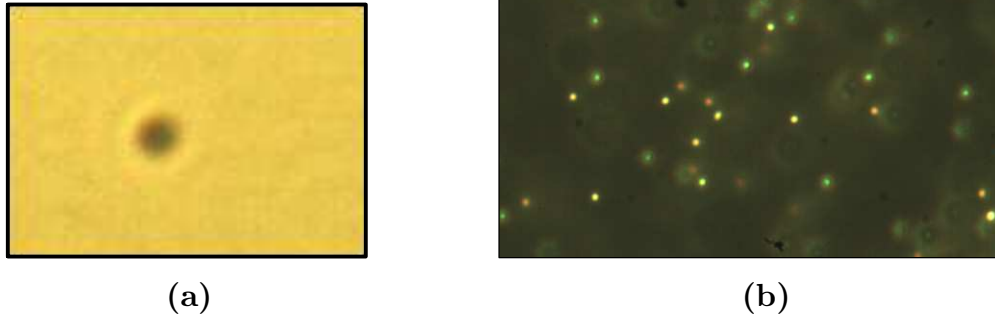


Fig. 3.8: Polystyrene particles with a diameter of 400 nm; (a) Bright-field image; (b) Dark-field image.

setup alignment and the subsequent subtraction of the corresponding background. In Fig. 3.9 we show the scattering spectra of the optically trapped polystyrene particle for 8 different distances of the dark-field Köhler illumination from the sample plane. The scattering intensities are naturally changing for different positions but also the peak position is shifting. Illuminating with the dark-field setup closer to the sample (from $-200\ \mu\text{m}$ to $-50\ \mu\text{m}$) the scattering spectra are blue-shifted – the peaks are in shorter wavelengths. On the other hand, if the illumination is further from the sample plane (from $50\ \mu\text{m}$ to $150\ \mu\text{m}$), the scattering spectra are red-shifted – the peak appears in longer wavelengths. This peak shifts can be evident from the dark-field images shown below the graph in Fig. 3.9. Colours are varying from orange to yellow–green. These measurements demonstrate that scattering spectra of any particle can be highly sensitive to the dark-field illumination alignment. Therefore it is necessary to fix the illumination position for all measurements otherwise we could not compare different spectrum records.

For the following measurements, the illumination was set into the position for the highest intensity of the light scattered by the polystyrene spheres (the distance $0\ \mu\text{m}$ in Fig. 3.9). We optically trapped the polystyrene particles one by one and recorded corresponding spectra, see Fig. 3.10a. The laser power was again approximately $40\ \text{mW}$ and each spectrum was recorded for $2\ \text{s}$. The plotted spectra were obtained by averaging 10 measured spectra of the same number of particles with the subtracted background. The profile of the scattering spectrum and the peak position remained unchanged, only the scattering intensity was increasing with the increasing number of the polystyrene particles. It means that there is no coupling between the trapped polystyrene particles. The acquired scattering peak intensity in dependence on the number of particles is shown in Fig. 3.10b (blue points). It is clear that the

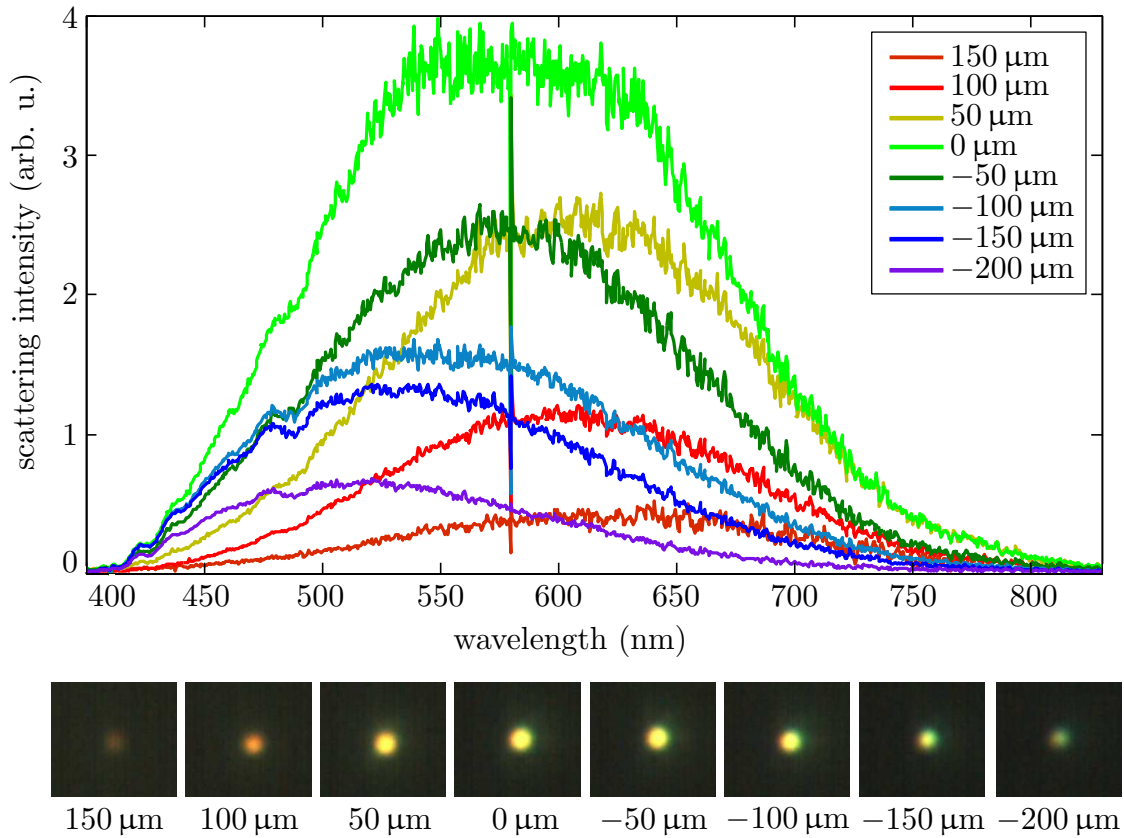


Fig. 3.9: Scattering spectra of a single polystyrene particle for different distances of the illumination settings. The scattering peaks for the shorter distances of the illumination settings from the sample plane (from $-200\ \mu\text{m}$ to $-50\ \mu\text{m}$) shift to the shorter wavelengths. Below the graph, dark-field images of the trapped particle are depicted. The distances are relative to the illumination position with the highest scattering intensity that was later used for all measurements.

peak intensity is directly proportional to the number of the trapped particles. The red line represents the fit obtained by the least-square method and we can see that the blue points representing the experimental data lie approximately on the fitting curve. The standard deviations marked with the black lines are relatively small, for lower numbers of particles the deviation is negligible, therefore the number of the trapped particles can be with certainty determined from the scattering intensity.

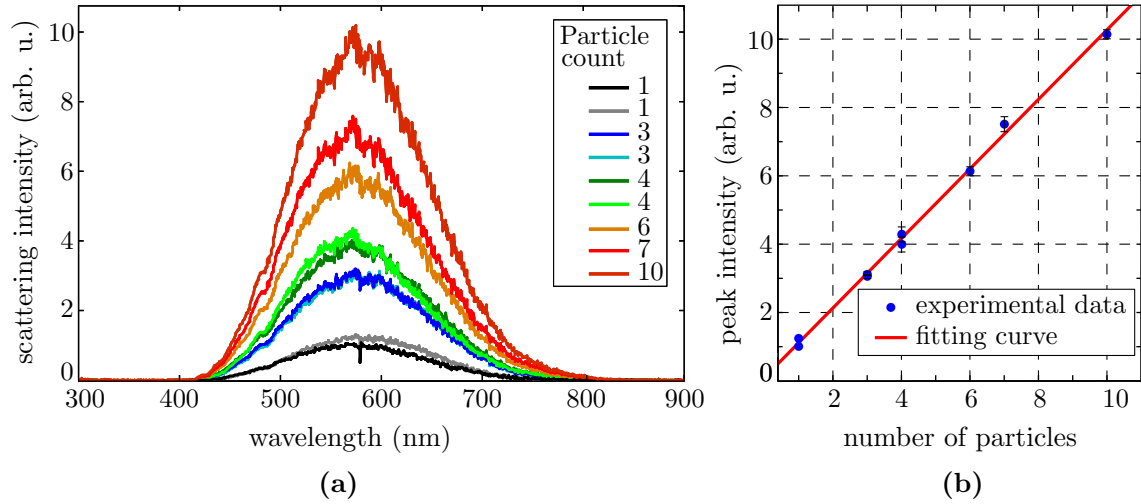


Fig. 3.10: (a) Scattering spectra of various numbers of trapped polystyrene particles with a diameter of 400 nm; (b) The scattering peak intensity of the spectra in (a) in dependence on the number of the trapped polystyrene particles. Blue dots represent experimental data and the red line is the fit obtained by the least-square method. The standard deviations are determined from ten measurements. For lower numbers of polystyrene particles the standard deviations are negligible.

3.2.2 The light scattered by silver nanoparticles

Using polystyrene particles we showed that we can perform the dark-field imaging, the optical trapping of particles in an aqueous solution and the recording of their scattering spectra. So now we can move ahead toward plasmonic particles and a characterization of their optical properties. We started with silver (Ag) nanoparticles with a diameter of 80 ± 7 nm (EM.SC80 BBI Solutions [73]). The nanoparticles are covered by the reduction agent – citric acid (2-hydroxypropane-1,2,3-tricarboxylic acid $C_6H_8O_7$) that prevents the nanoparticles from their agglomeration.

The sample of Ag nanoparticles was prepared in the same way as the sample of the polystyrene particles. The diluted solution of Ag nanoparticles was applied on the slide with the 0.1mm thick spacer and was covered by the cover glass. The cover-glass edges were closed by a nail polish to prevent the sample from drying and the

fluid flow. The prepared sample was placed the cover glass downwards between the objective and the condenser lens with the immersion oil. The illumination settings was aligned into the position of the highest scattering intensity of the polystyrene spheres (the distance $0\ \mu\text{m}$ in Fig. 3.9).

The dark-field image of the denser solution of Ag nanoparticles is depicted in Fig. 3.11a. The colours of the nanoparticles correspond to the resonant wavelengths of plasmonic oscillations in the nanoparticles. The nanoparticles are differently coloured, from light blue to yellow-orange. This behaviour can be partially caused by the distance of the nanoparticles from the illumination settings, as we discussed above in section 3.2.1, and then the profile of the illumination spectrum might determined the dominant colour. But as the focused nanoparticles are in the same distances from the illumination setup, this varicoloured performance is mostly caused by the heterogeneity of the colloidal solution. In Fig. 3.11b, the image of the Ag solution taken by the scanning electron microscope (SEM) is depicted. Different sizes and shapes of nanoparticles can be observed. Even if the standard deviation of their size is $7\ \text{nm}$ we can find in the solution some Ag nanoparticles that differ from the specified dimension and the spherical shape much more and thus the plasmonic oscillations are set into the different frequencies.

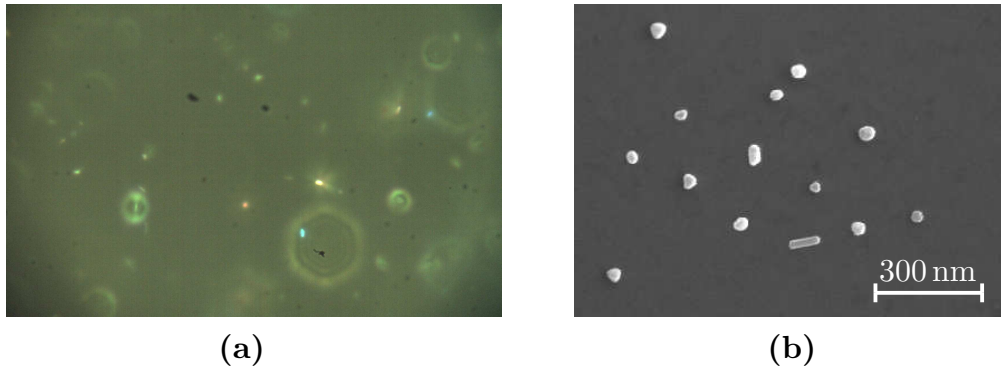


Fig. 3.11: (a) Dark-field image of the colloidal solution of silver nanoparticles with the average diameter of $80\ \text{nm}$; (b) SEM image of Ag nanoparticles from the solution on the silicon substrate. Different sizes and shapes can be observed, taken by Ing. Zdena Druckmüllerová.

All scattering spectra presented in this section were proceeded in the following way. At first the recorded spectra were $10\times$ averaged and subsequently the background was subtracted. Then the obtained spectrum was divided by the illumination spectrum plotted in Fig. 3.6 to correct the scattering spectrum for the spectral variations in the optical system. In Fig. 3.12, the normalized scattering spectra of differently coloured Ag nanoparticles are plotted. We optically trapped several Ag nanoparticles of the same colour (The trapping-laser power was approximately $200\ \text{mW}$

in front of the filter.) and recorded one scattering spectrum for 10s. From the graph in Fig. 3.12 we see that the peak position for differently coloured nanoparticles is significantly shifted, from 472 nm to 530 nm. The corresponding dark-field images of the trapped nanoparticles are shown below the graph. The colours approximately correspond to the resonant wavelengths in the scattering spectra, from light blue to yellow-green. The red circle in the left image indicates the collection area. Since the camera and the spectrometer were approximately in the same distances from the tube lens, the size of the red circle was estimated from the spectrometer-fibre diameter (200 μm) and the size of the camera pixel (5.5 μm). Even if the collection area is relatively small and involves mostly only the trapped nanoparticle, it is necessary to have the highly diluted colloidal solution in order to avoid the optical trapping of another object during the spectrum recording and to suppress the scattering from nearby nanoparticles.

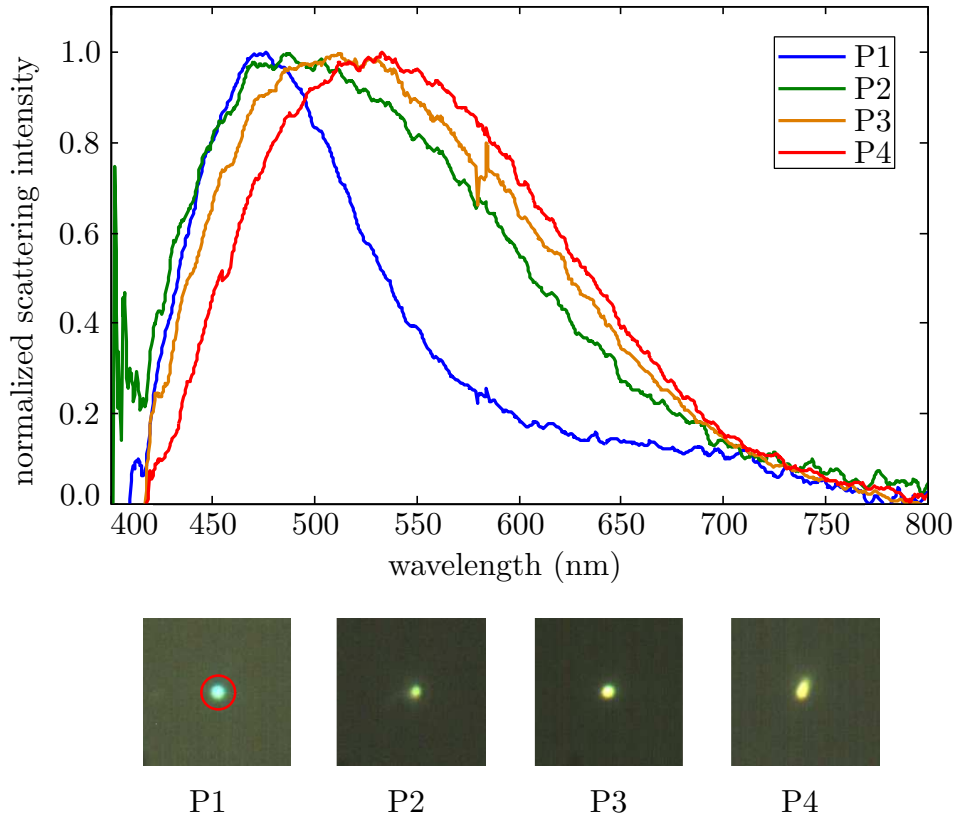


Fig. 3.12: The normalized scattering spectra of Ag nanoparticles with different peak positions. The plotted curves are corrected for the system spectral variations. The corresponding dark-field images are shown below the graph. The red circle indicates the estimated collection area.

Then we optically trapped the nanoparticle of the most frequent colour, green one. We cannot with certainty claim that it was only one Ag particle or i.e. its

dimer, but we tried to trap the objects with the lowest scattering intensity we could distinguish in the camera image. We recorded the scattering spectrum for 20s and proceeded the acquired data as described above. The received spectrum was normalized to the calculated scattering intensity (see Fig. 3.13). Because the nanoparticles are of the spherical shape we could apply the Mie theory for the theoretical calculations. For that purpose we used the open-source code written by Ch. Mätzler in MATLAB [74]. This code utilizes the formalism of C. F. Bohren and D. R. Huffman [40] described in section 2.3.2. The refractive indices were taken from the book written by E. D. Palik [75]. The number n of summarized terms is approximately given by the wave number k of the incident light and the radius a of the sphere:

$$n \doteq 2 + x + 4x^{1/3}, \quad (3.11)$$

where x is the size parameter defined as $x = ka$. If we compare the calculated and the measured scattering intensity, the peak position fits well and the profile of the measured scattering intensity in the longer wavelengths follow the behaviour of the simulated spectrum. In shorter wavelengths we cannot compare these two spectra because the illumination intensity in shorter wavelength than approximately 450 nm is practically negligible (see Fig. 3.6). However, the calculated profile of the scattering intensity slightly differs from the experimental data in longer wavelengths, too. This behaviour can be probably caused by the particle shapes. Since the Ag nanoparticles are not ideal spheres but they are significantly deformed, the scattering-intensity profile can have slightly different trend. Differences in the experimental and the calculated data can be also caused by inaccurate calculations. The shape and the position of the scattering peak can be affected by the choice of the refractive indices. The dielectric function values from different sources can give slightly different results for the scattering spectra [76].

The peak broadening can be achieved by the optical trapping of the multiple metallic nanoparticles (demonstrated for example by L. Ling et al. [63]). We optically trapped the single Ag nanoparticle (the object with the lowest intensity) and recorded the scattering spectrum for 10s. Then we trapped another particle from the solution and recorded the scattering spectrum again. In this way we continued step-by-step with other Ag nanoparticles. We tried to trapped the nanoparticles of the same colour therefore they should have the similar optical characteristics. In Fig. 3.14 and Fig. 3.15 the normalized scattering intensities for the various number of the trapped object are plotted. For the low particle count, the spectrum profile is almost identical. If we add more object into the optical trap, the scattering peak gets broaden. The peak broadening for seven and ten objects is nearly the same. For even higher particle count the peak broadening stays unchanged. There are two

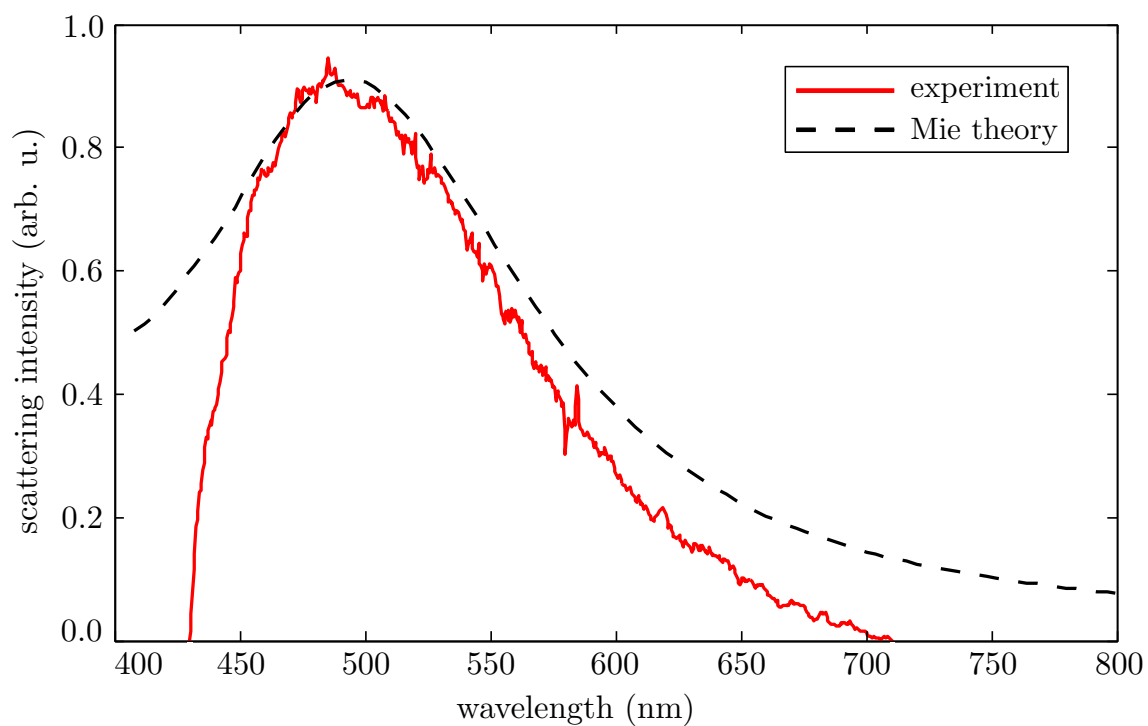


Fig. 3.13: The experimentally obtained scattering spectrum of the smallest visible green object from the Ag colloidal solution normalized to the calculated scattering spectrum. The profile of the experimental data is corrected for the system spectral variations. The red solid line represents the experimental data and the black dashed line represents calculated spectrum.

main factors that can affect this peak broadening. The first one is the shape heterogeneity of the trapped nanoparticles. We tried to minimize this contribution to the peak broadening by picking the Ag particles of the same colour. The other cause of the peak broadening is the interparticle coupling [15]. The distances between the particles in the optical trap are very short and therefore the nanoparticles can interact with each other [63]. To the peak broadening, the position of the trapped particles can partially contribute (as discussed above). The nanoparticles can be trapped inline and create a chain. But the length of this chain is only about $1\ \mu\text{m}$ therefore the chromatic aberration should not play a significant role.

The peaks in Fig. 3.15 are generally narrower compared to the scattering spectra in Fig. 3.14. It is given by the illumination profile where the intensity for shorter wavelengths than 500 nm rapidly decreasing (see Fig. 3.6). Despite this limitation, the peak broadening in Fig. 3.15 can be clearly observed.

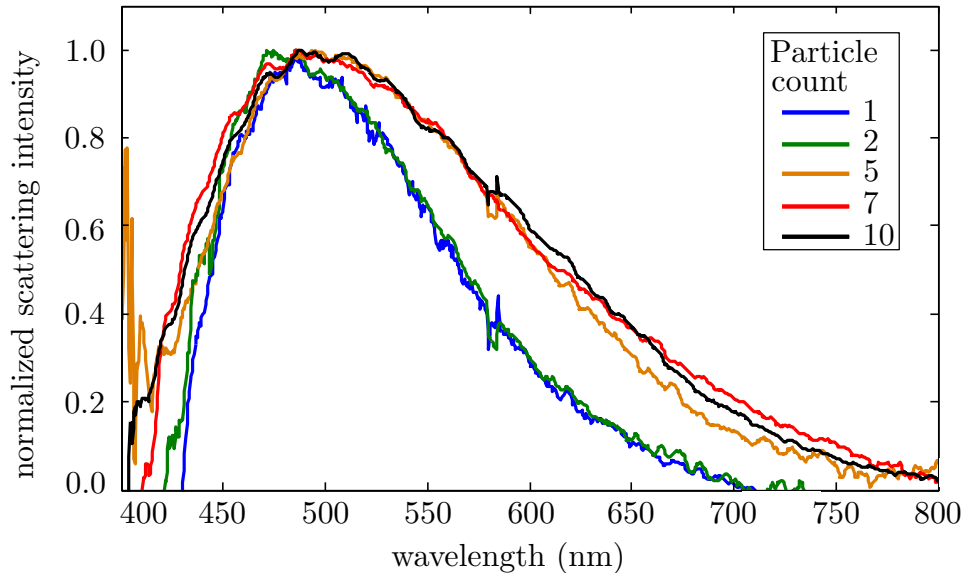


Fig. 3.14: The normalized scattering spectra of the different particle counts. For more particles the peak is significantly broader. The scattering spectra are corrected for the system spectral variations.

In Fig. 3.16a we plot the unnormalized scattering spectra for the different particle counts used in Fig. 3.14. The scattering intensity is higher for the higher particle count. In Fig. 3.16b the dependence of the scattering-peak intensity on the particle count is plotted (blue points). This dependence is clearly linear, as well as for the polystyrene particles. The red line represents the fit obtained by the least-square method. The blue points representing the experimental data lie approximately on the fitting line. The standard deviations is negligible compared to the intensity

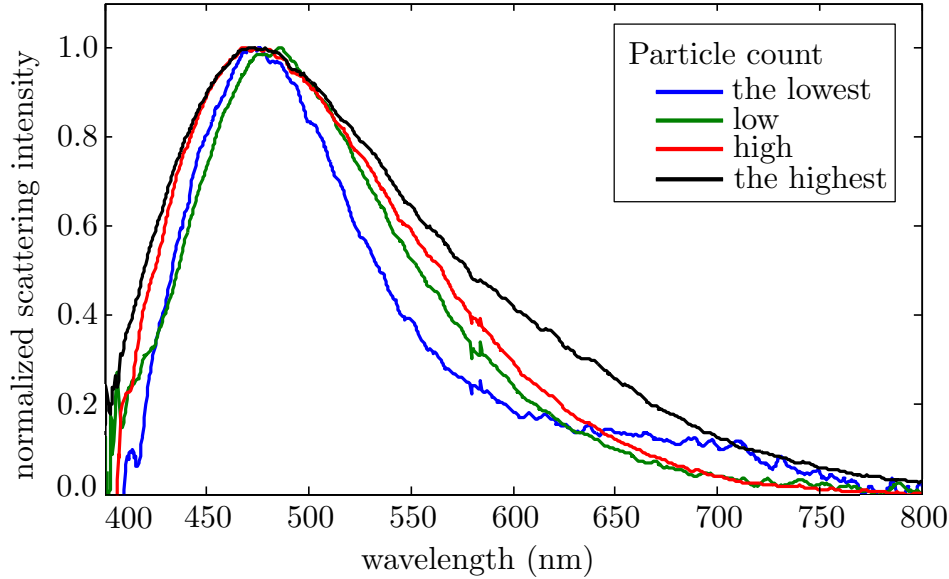


Fig. 3.15: The normalized scattering spectra of the different particle counts. For more objects, the peak is significantly broader. The rapid decrease in the scattering intensities in shorter wavelengths is caused by the illumination-intensity profile. The scattering spectra are corrected for the system spectral variations.

values and therefore the trapped-particle count can be estimated from the scattering intensity.

The characterization of the optical properties of the silver nanoparticles was relatively successful. We were able to stably trap a single object or a desired number of them and record the scattering spectra of the optically trapped nanoparticles. The dark-field images and the corresponding scattering spectra demonstrated the heterogeneity of the colloidal solution. The scattering intensity gave the information about the trapped particle count and thus the number of the trapped nanoparticles can be easily estimated in this way. The profile of the scattering spectrum varied with the particle count. The more particles, the wider scattering peak. The reason for this behaviour could be the interparticle coupling and the particle-shape heterogeneity.

3.2.3 Optical spectroscopy of gold nanoparticles

Since we were able to measure the scattering spectrum of the single and multiple silver nanoparticles, we started with the optical characterization of gold (Au) colloidal solutions. The Au colloidal solutions were prepared by Ing. F. Novotný at CTU in Prague using the seeded growth method [77]. For the nanoparticle formation, the surfactant CTAB (hexadecyltrimethylammonium bromide $(C_{16}H_{33})N(CH_3)_3Br$) was

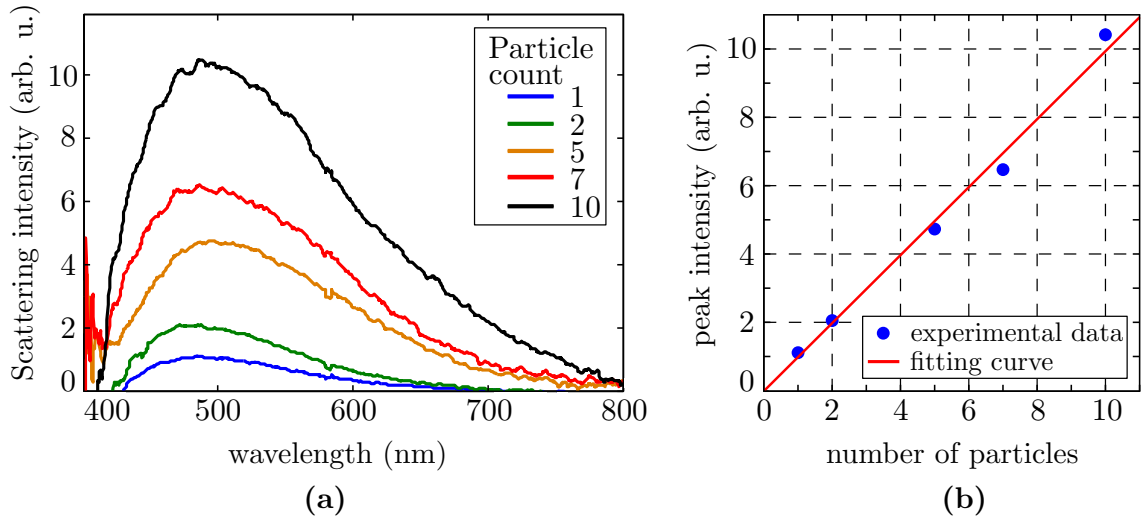


Fig. 3.16: (a) Scattering spectra of various numbers of trapped Ag nanospheres with a diameter of approximately 80 nm; (b) The scattering peak intensity of the spectra in (a) in dependence on the number of trapped Ag nanoparticles. Blue dots represent experimental data and the red line is the fit obtained by the least-square method.

used and the Au nanorods of the following dimensions were grown: $(26 \pm 4) \text{ nm} \times (54 \pm 6) \text{ nm}$, $(25 \pm 4) \text{ nm} \times (76 \pm 11) \text{ nm}$ and $(97 \pm 8) \text{ nm} \times (146 \pm 11) \text{ nm}$, where the first dimension is the base size. In Fig. 3.17a the SEM image of the smallest Au nanorods ($26 \text{ nm} \times 54 \text{ nm}$) is depicted. The solution contained mostly Au nanoparticles of the desired shape and dimensions and the homogeneity of nanoparticle features was significant.

To know what scattering spectra we should expect from these colloidal solutions, we applied the numerical calculations. Since the shape of the nanoparticles is not spherical or ellipsoidal, we had to use the ADDA method described in section 2.3.3. We calculated scattering cross sections of gold nanoparticles in an aqueous solution. The simulated objects were nanorods with square bases and their dimensions were given by the fabricated nanorods, it means $26 \text{ nm} \times 54 \text{ nm}$, $25 \text{ nm} \times 76 \text{ nm}$ and $97 \text{ nm} \times 146 \text{ nm}$. The distance between the dipoles was set on 0.7 nm for two smaller particles and for the longest one the interdipole distance was 1.5 nm. We studied the scattering cross sections of gold particles illuminated by a plane wave propagating in the z -axis direction and polarized in the y -axis direction. We considered three orientations of a nanoparticle, the long axis of a nanoparticle parallel with the axes of the Cartesian coordinate system. The dielectric functions of gold and water were taken from Sopra S.A. [78]. The accuracy of the numerical calculations was $10^{-4} \%$.

In Fig. 3.18 the scattering cross sections for all three positions of the Au nanorod with dimensions $97 \text{ nm} \times 146 \text{ nm}$ are plotted. If the polarization direction of the

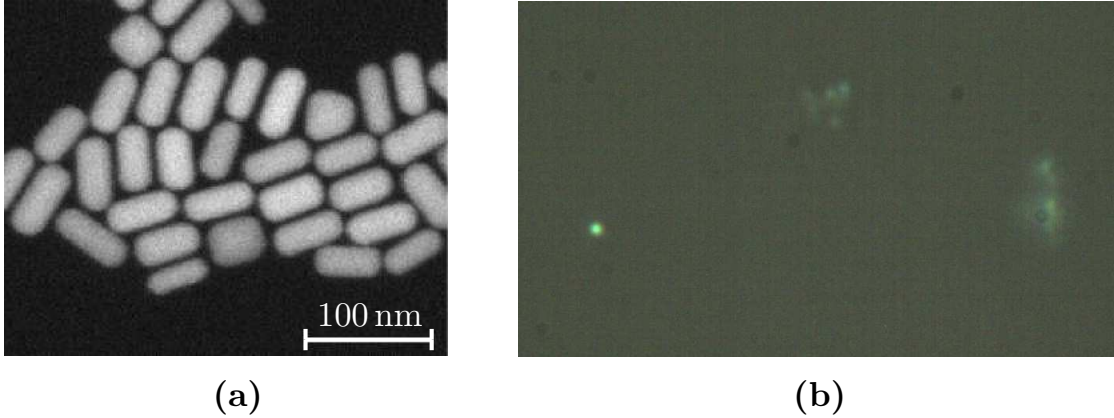


Fig. 3.17: (a) SEM image of the colloidal solution of the Au nanorods with dimensions of $26 \text{ nm} \times 54 \text{ nm}$; taken by Ing. Filip Novotný; (b) Dark-field image of the colloidal solution of the Au nanorods with the dimensions of $97 \text{ nm} \times 146 \text{ nm}$.

incident electromagnetic wave is parallel with the long nanorod axis (black line), the longitudinal mode (LM) is generated. On the other hand, if the incident-light polarization direction is parallel with the short nanorod axis (red and blue lines), the transversal modes (TM) are excited. As we supposed on the basis of the described theory in section 2.3.4, the scattering peak of the longitudinal mode is situated at the longer wavelengths compare to the transversal modes. The LM scattering intensity is significantly higher than for the transversal modes and the scattering LM peak is broader.

In Fig. 3.19 we compare the calculated scattering cross sections for all three nanorods oriented parallel to the y axis (excitation of LM). The scattering peak for the smaller nanorod is at the shorter wavelengths and the scattering intensity is much lower (Note that the scale for the scattering cross section is logarithmic.). All calculated spectra have the scattering peaks in the visible region or near-infrared region, that satisfies the requirement given by the transparent window of the dichroic mirror used in the optical setup (see Fig. 3.5).

Before the dark-field imaging and the optical spectroscopy of the Au nanoparticles, the colloidal solutions had to be properly prepared. Since the gold nanoparticles formed into the large clusters, we used the 1% solution of sodium dodecyl sulfate ($\text{CH}_3(\text{CH}_2)_{11}\text{OSO}_3\text{Na}$) to prevent the nanoparticles from agglomerations. After applying the prepared solution on the slide, the Au nanoparticles attached in a little time to the glass substrate. Therefore we applied the siliconizing reagent Sigmacote [79] on the slide and the cover glass and then the nanoparticles stucked to the surface much less.

The sample for the dark-field imaging was prepared in the same way like the

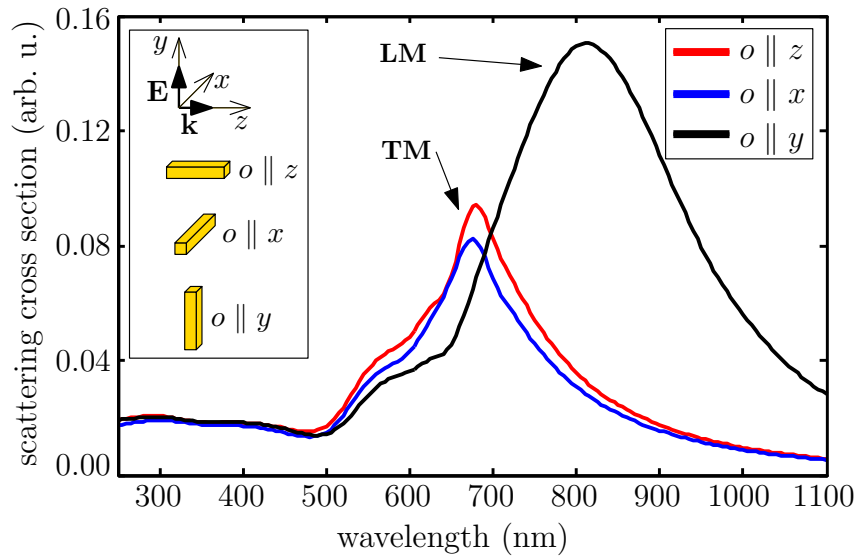


Fig. 3.18: The scattering cross section in dependence on the wavelength of the incident light calculated by ADDA method. The spectra are calculated for the $97 \text{ nm} \times 146 \text{ nm}$ Au nanorod oriented parallel ($o \parallel y$) and perpendicular ($o \parallel z$, $o \parallel x$) to the polarization direction of the incident light. If the long nanorod axis is parallel with the polarization direction, the longitudinal (LM) mode is excited. If the long nanorod axis is perpendicular to the polarization direction, the transversal modes (TM) are excited.

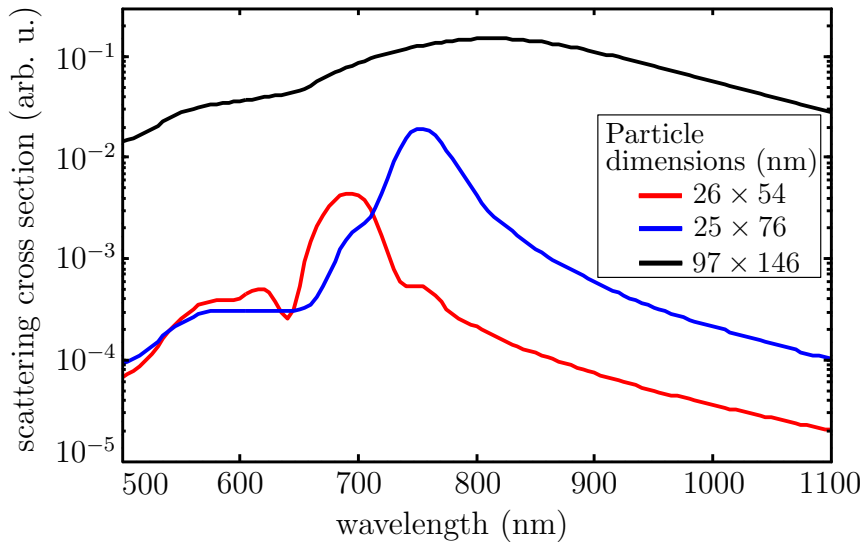


Fig. 3.19: The scattering cross section in dependence on the wavelength of the incident light calculated by ADDA method. The spectra are calculated for the different Au nanorods with the long axis parallel with the polarization direction of the incident light.

sample with the silver colloidal solution. The illumination settings was aligned into the same position. In Fig. 3.17b we show the dark-field image of the colloidal solution with the Au nanoparticles with the dimensions of $97 \text{ nm} \times 146 \text{ nm}$. The nanoparticles were often clustered (It can be seen also in the dark-field image.) but sometimes we observed much smaller nanoparticles. These nanoparticles had very low intensity that was close to the noise level. Since the nanoparticles were very small, the trap stiffness was low and the nanoparticles could not be easily trapped in the optical tweezers (see section 3.1.1). Thus we tried to record the scattering spectrum of the nanoparticle stucked to the glass surface. But the scattering intensity was very low and the spectrometer was not sensitive enough for this purpose.

The larger clusters could be optically trapped and also the scattering intensity was higher. The nanorods in the optical trap can be aligned parallel or perpendicular to the trapping-laser polarization direction. For the laser wavelength that we used for the optical trapping and the aspect ratios of the investigated nanoparticles, the nanoparticle alignment should be parallel with the polarization direction [80]. We recorded the optical spectrum of the trapped object with the illumination-polarization direction parallel to the polarization direction of the trapping laser (see Fig. 3.20). The trapping-laser power was approximately 100 mW in front of the filter. If we compare the obtained spectrum (red line) with the illumination spectrum (blue line), the scattering peak is in the same position as the intensity maximum of the illumination. This result repeated for any illumination-polarization direction and for all three prepared solutions with the different dimensions of the nanoparticles. The nanoparticles could attach to each other and form larger objects. Thus the scattering peak would be shifted into the longer wavelengths in the infrared region where our setup is not sensitive. In the visible region, the scattering spectrum of the trapped object just followed the illumination-intensity profile. Up to now, we have tried to improve the setup alignment and the sample preparation. We have improved the optical components and optimized the numerical aperture of the objective together with the diameter of the dark-field annulus but the measurements have not been successfully performed yet.

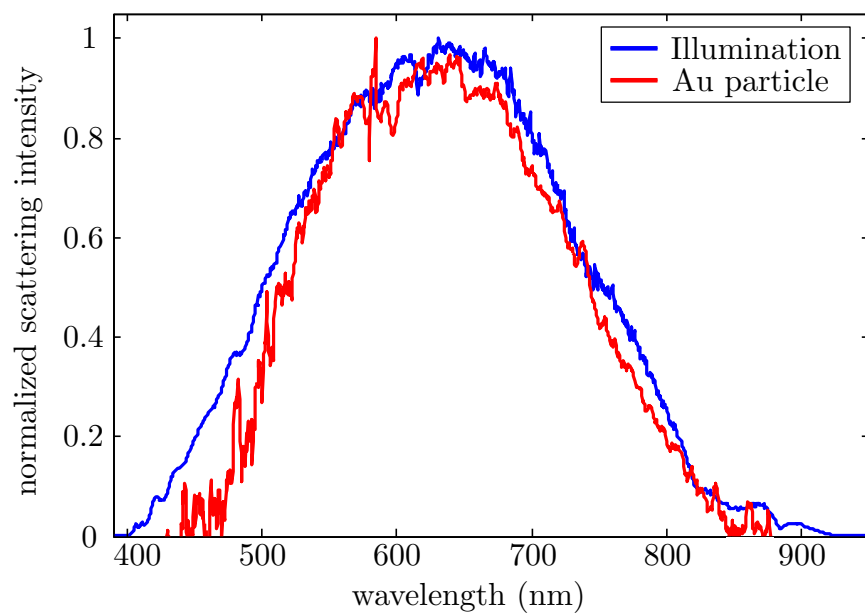


Fig. 3.20: The normalized scattering spectrum of a cluster of the Au nanoparticles with the dimensions of $97 \text{ nm} \times 146 \text{ nm}$ (red line). The spectrum was recorded for 20 s. The blue line represents the normalized illumination spectrum.

4 CONCLUSIONS

This thesis reports on the investigation of the optical responses of polystyrene and metallic particles. Metallic nanoparticles are widely utilized in the nanooptics applications e.g. in biosensing, microscopy and optoelectronics, especially for their unique optical properties originating in the localized-surface-plasmon resonances. Silver and gold nanoparticles are chemically stable and their resonance frequencies are typically set in the visible range, therefore these metallic nanoparticles are objects of an active research. The resonance wavelengths are strongly dependent on the nanoparticle size and shape. In some applications, just a single particle is used and therefore there is a demand on the investigation of the isolated-nanoparticle optical characteristics. For that purpose, the optical trapping combined with the optical spectroscopy can be utilized to characterize the nanoparticles in a solution.

As a part of this thesis, we designed and tested the optical setup suitable for measurements of the scattering spectra of the optically trapped plasmonic nanoparticles. It consisted of three branches: optical tweezers, dark-field illumination and a branch for a detection of the scattered light. The optical trapping was performed using a single-beam gradient trap created by an inverted microscope focusing the laser beam ($\lambda = 1064 \text{ nm}$) into the sample plane. The dark-field illumination using halogen lamp as a white-light source was of the Köhler type. The light scattered by the trapped particles in the colloidal solution was collected and focused into the spectrometer and the camera.

The proper alignment of the optical setup was tested using spherical polystyrene particles with a diameter of approximately 400 nm. In this thesis we pointed out to the illumination-spectrum dependence on the dark-field illumination setting position and consequently also the polystyrene scattering spectrum dependence on the illumination-setting position. This spectral variation was caused by the chromatic aberration of the illumination system. However, since nanoparticles are always trapped approximately in the same distances from objective used for the optical trapping and condenser lens used for the dark-field illumination, the scattering spectra could be corrected for the spectral variations of the optical system and therefore the measurements were reproducible. It was proved that the scattering intensity of the polystyrene particles was directly proportional to the number of the optically trapped particles.

Then we investigated the optical responses of the silver spherical nanoparticles with a diameter of approximately 80 nm. Using a scanning electron microscope it was found that the nanoparticles were of the various shapes and sizes. Thus the scattering-peak positions representing the LSP resonance wavelengths were shifted and in the dark-field image we could observe differently coloured nanoparticles. The

scattering spectrum of the Ag nanoparticle with the most frequent colour (green one) was compared with the theoretical calculations following the Mie theory. We found a good agreement between the experimental data and the Mie solution. Slight differences were probably caused by the nanoparticle shape and size that could differ from the ideal spherical object for which the Mie theory is derived.

As well as for the polystyrene particles, the scattering intensity of the silver nanoparticles was directly proportional to the trapped-nanoparticle count, but the scattering-intensity profile was varying for the increasing number of the trapped nanoparticles. The distances between the optically trapped particles were too short and therefore the nanoparticles started to interact with each other. This interparticle coupling caused the broadening of the resonance scattering peak for a higher number of the trapped nanoparticles.

Consequently we investigated the scattering properties of the gold nanoparticles. Using the DDA method, we theoretically studied scattering cross sections of three nanorods with different dimensions illuminated with a linearly polarized plane wave. If the illumination-polarization direction was perpendicular to the nanorod long axis, transversal modes were excited, where for the polarization direction parallel to the nanorod long axis the longitudinal modes were excited. The longitudinal modes had generally higher intensities and were shifted to longer wavelengths compared to the transversal modes. For shorter nanorods, the scattering intensity of the LM peak was lower and shifted to shorter wavelengths.

Since the Au nanoparticles in an aqueous solution exhibited very low scattering intensity, only clustered object could be seen in the dark-field image and consequently analysed by the spectrometer. But if we recorded the scattering spectrum of the Au cluster, it had approximately the same profile as the illumination spectrum. The scattering peak for significantly larger objects is shifted into the near infrared region where our setup is not sensitive and therefore we recorded only the faint reflection of the illumination spectrum.

The next steps of this work will be to improve the optical setup in order to increase the sensitivity for lower scattering intensities. This could be performed by implementation of better quality components, especially a spectrometer with higher sensitivity. As we will have obtained high enough scattering intensity, we will compare scattering-intensity profiles in dependence on the nanorod size and the illumination-polarization direction.

BIBLIOGRAPHY

- [1] Ritchie, R. H.: Plasma Losses by Fast Electrons in Thin Films. *Physical Review*. 1957, 106(5):874–881.
- [2] Powell, C. J. and Swan, J. B.: Effect of Oxidation on the Characteristic Loss Spectra of Aluminum and Magnesium. *Physical Review*. 1960, 118(3):640–643.
- [3] Novotny, L. and Hecht, B.: *Principles of Nano - Optics*. New York: Cambridge University Press, 2006. 558 p. ISBN 0-521-83224-1.
- [4] Mie, G.: Beiträge zur Optik trüber Medien, speziell kolloidaler Metallösungen. *Annalen der Physik*. 1908, 330(3):377–445.
- [5] Barnes, W. L., Dereux, A., and Ebbesen, T. W.: Surface Plasmon Subwavelength Optics. *Nature*. 2003, 424:824–830.
- [6] Haynes, Ch. L. and Van Duyne, R. P.: Nanosphere Lithography: A Versatile Tool for Studies of Size-Dependent Nanoparticle Optics. *The Journal of Physical Chemistry B*. 2001, 105(24):5599–5611.
- [7] Mock, J. J., Barbic, M., Smith, D. R., Schultz, D. A., and Schultz, S.: Shape Effects in Plasmon Resonance of Individual Colloidal Silver Nanoparticles. *The Journal of Chemical Physics*. 2002, 116(15):6755.
- [8] Link, S. and El-Sayed, M. A.: Spectral Properties and Relaxation Dynamics of Surface Plasmon Electronic Oscillations in Gold and Silver Nanodots and Nanorods. *The Journal of Physical Chemistry B*. 1999, 103(40):8410–8426.
- [9] Karg, M., Lu, Y., Carbó-Argibay, E., Pastoriza-Santos, I., Pérez-Juste, J., Liz-Marzán, L. M., and Hellweg, T.: Multiresponsive Hybrid Colloids Based on Gold Nanorods and Poly(NIPAM-co-allylactic acid) Microgels: Temperature- and pH-Tunable Plasmon Resonance. *Langmuir*. 2009, 25(5):3163–3167.
- [10] Brzobohatý, O., Šiler, M., Trojek, J., Chvátal, L., Karásek, V., Paták, A., Pokorná, Z., Mika, F., and Zemánek, P.: Three-Dimensional Optical Trapping of a Plasmonic Nanoparticle using Low Numerical Aperture Optical Tweezers. *Scientific Reports*. 2015, 5:8106.
- [11] Hanarp, P., Käll, M., and Sutherland, D. S.: Optical Properties of Short Range Ordered Arrays of Nanometer Gold Disks Prepared by Colloidal Lithography. *The Journal of Physical Chemistry B*. 2003, 107(24):5768–5772.

- [12] Hentschel, M., Gregely, D., Vogelgesang, R., Giessen, H., and Liu, N.: Plasmonic Oligomers: The Role of Individual Particles in Collective Behavior. *ACS Nano*. 2001, 5(3):2042–2050.
- [13] Novo, C., Funston, A. M., and Mulvaney, P.: Direct Observation of Chemical Reactions on Single Gold Nanocrystals using Surface Plasmon Spectroscopy. *Nature Nanotechnology*. 2008, 3:598–602.
- [14] Link, S. and El-Sayed, M. A.: Size and Temperature Dependence of the Plasmon Absorption of Colloidal Gold Nanoparticles. *The Journal of Physical Chemistry*. 1999, 103(21):4212–4217.
- [15] Prikulis, J., Svedberg, F., Käll, M., Enger, J., Ramser, K., Goksör, M., and Hanstorp, D.: Optical Spectroscopy of Single Trapped Metal Nanoparticles. *Nano Letters*. 2004, 4(1):115–118.
- [16] Tong, L., Miljković, V. D., and Käll, M.: Alignment, Rotation, and Spinning of Single Plasmonic Nanoparticles and Nanowires Using Polarization Dependent Optical Forces. *Nano Letters*. 2010, 10:268–273.
- [17] Xiong, Y., McLellan, J. M., Chen, J., Yin, Y., Li, Z.-Y., and Xia, Y.: Kinetically Controlled Synthesis of Triangular and Hexagonal Nanoplates of Palladium and Their SPR/SERS Properties. *Journal of the American Chemical Society*. 2005, 127(48):17118–17127.
- [18] Xiong, Y., Chen, J., Wiley, B., Xia, Y., Yin, Y., and Li, Z.-Y.: Size-Dependence of Surface Plasmon Resonance and Oxidation for Pd Nanocubes Synthesized via a Seed Etching Process. *Nano Letters*. 2005, 5(7):1237–1242.
- [19] Nie, S. and Emory, S. R.: Probing Single Molecules and Single Nanoparticles by Surface-Enhanced Raman Scattering. *Science*. 1997, 275(5303):1102–1106.
- [20] Félidj, N., Aubard, J., Lévi, G., Krenn, J. R., Hohenau, A., Schider, G., Leitner, A., and Aussenegg, F. R.: Optimized Surface-Enhanced Raman Scattering on Gold Nanoparticle Arrays. *Applied Physics Letters*. 2003, 82:3095–3097.
- [21] Neubrech, F., Kolb, T., Lovrincic, R., Fahsold, G., Pucci, A., Aizpurua, J., Cornelius, T. W., Toimil-Molares, M. E., Neumann, R., and Karim, S.: Resonances of Individual Metal Nanowires in the Infrared. *Applied Physics Letters*. 2006, 89:253104.
- [22] Kneipp, K., Wang, Y., Kneipp, H., Perelman, L. T., Itzkan, I., Dasari, R. R., and Feld, M. S.: Single Molecule Detection Using Surface-Enhanced Raman Scattering (SERS). *Physical Review Letters*. 1997, 78(9):1667–1670.

- [23] Neubrech, F., Pucci, A., Cornelius, T. W., Karim, S., García-Etxarri, A., and Aizpurua, J.: Resonant Plasmonic and Vibrational Coupling in a Tailored Nano-antenna for Infrared Detection. *Physical Review Letters*. 2008, 101(15):157403.
- [24] Schultz, D. A.: Plasmon Resonant Particles for Biological Detection. *Current Opinion in Biotechnology*. 2003, 14(1):13–22.
- [25] Oldenburg, S. J., Genick, C. C., Clark, K. A., and Schultz, D. A.: Base Pair Mismatch Recognition Using Plasmon Resonant Particle Labels. *Analytical Biochemistry*. 2002, 309(1):109–116.
- [26] Levi, S. A., Mourran, A., Spatz, J. P., Veggel, F. C. van, Reinhoudt, D. N., and Möller, M.: Fluorescence of Dyes Adsorbed on Highly Organized, Nanostructured Gold Surfaces. *Chemistry*. 2002, 8(16):3808–3814.
- [27] Chen, Y., Munechika, K., and Ginger, D. S.: Dependence of Fluorescence Intensity on the Spectral Overlap between Fluorophores and Plasmon Resonant Single Silver Nanoparticles. *Nano Letters*. 2007, 7(3):690–696.
- [28] El-Sayed, I. H., Huang, X., and El-Sayed, M. A.: Surface Plasmon Resonance Scattering and Absorption of anti-EGFR Antibody Conjugated Gold Nanoparticles in Cancer Diagnostics: Applications in Oral Cancer. *Nano Letters*. 2005, 5(5):829–834.
- [29] Liao, H., Nehl, C. L., and Hafner, J. H.: Biomedical Applications of Plasmon Resonant Metal Nanoparticles. *Nanomedicine*. 2006, 1(2):201–208.
- [30] Salerno, M., Krenn, J. R., Lamprecht, B., Schider, G., Ditlbacher, H., Félidj, N., Leitner, A., and Aussenegg, F. R.: Plasmon Polaritons in Metal Nanostructures: The Optoelectronic Route to Nanotechnology. *Opto - Electronics Review*. 2002, 10(3):217–224.
- [31] Bludov, Y. V., Vasilevskiy, M. I., and Peres, N. M. R.: Mechanism for Graphene-Based Optoelectronic Switches by Tuning Surface Plasmon - Polaritons in Monolayer Graphene. *Europhysics Letters*. 2010, 92(6):68001.
- [32] Wang, G., Lu, H., Liu, X., Mao, D., and Duan, L.: Tunable Multi-Channel Wavelength Demultiplexer Based on MIM Plasmonic Nanodisk Resonators at Telecommunication Regime. *Optics Express*. 2011, 19(4):3513–3518.
- [33] Mattiucci, N., D’Aguanno, G., and Bloemer, M. J.: Long Range Plasmon Assisted All-Optical Switching at Telecommunication Wavelengths. *Optics Letters*. 2012, 37(2):121–123.

- [34] Yelin, D., Oron, D., Thiberge, S., Moses, E., and Silberberg, Y.: Multiphonon Plasmon - Resonance Microscopy. *Optics Express*. 2003, 11(12):1385–1391.
- [35] Smolyaninov, I. I., Elliot, J., Zayats, A. V., and Davis, Ch. C.: Far - Field Optical Microscopy with a Nanometer - Scale Resolution Based on the In - Plane Image Magnification by Surface Plasmon Polaritons. *Physical Review Letters*. 2005, 94(5):057401.
- [36] Mulvaney, P.: Surface Plasmon Spectroscopy of Nanosized Metal Particles. *Langmuir*. 1996, 12(3):788–800.
- [37] Willets, K. A. and Van Duyne, R. P.: Localized Surface Plasmon Resonance Spectroscopy and Sensing. *Annual Review of Physical Chemistry*. 2007, 58:267–297.
- [38] Lu, X., Rycenga, M., Skrabalak, S. E., Wiley, B., and Xia, Y.: Chemical Synthesis of Novel Plasmonic Nanoparticles. *Annual Review of Physical Chemistry*. 2009, 60:167–192.
- [39] Dienerowitz, M., Mazilu, M., and Dholakia, K.: Optical Manipulation of Nanoparticles: A Review. *Journal of Nanophotonics*. 2008, 2:021875.
- [40] Bohren, C. F. and Huffman, D. R.: *Absorption and Scattering of Light by Small Particles*. New York: Wiley-VCH, 1998. 530 p. ISBN 0-471-29340-7.
- [41] Thidé, B.: *Electromagnetic Field Theory*. Uppsala: Dover Publications, 2011. 240 p. ISBN 0-486-47773-8.
- [42] Jackson, J. D.: *Classical Electrodynamics*. USA: Wiley-VCH, 1999. 811 p. ISBN 0-471-30932-X.
- [43] Dub, P. and Petráček, J.: *Vybrané problémy z teorie elektromagnetického pole*. [Course text.] Brno: VUT, FSI, 2009. 60 p.
- [44] Weber, W. H. and Merlin, R.: *Raman Scattering in Materials Science*. Berlin: Springer, 2000. 494 p. ISBN 3-540-67223-0.
- [45] Ni, W., Kou, X., Yang, Z., and Wang, J.: Tailoring Longitudinal Surface Plasmon Wavelengths, Scattering and Absorption Cross Sections of Gold Nanorods. *ACS Nano*. 2008, 2(4):677–686.
- [46] Maier, S. A.: *Plasmonics: Fundamentals and Application*. New York: Springer, 2007. 201 p. ISBN 0-387-33150-6.

- [47] Kalousek, R., Dub, P., Břínek, L., and Šikola, T.: Response of Plasmonic Resonant Nanorods: An Analytical Approach to Optical Antennas. *Optics Express*. 2012, 20(16):17916–17927.
- [48] Maloney, J. G., Smith, G. S., and Scott, W. R.: Accurate Computation of the Radiation from Simple Antennas using the Finite-Difference Time-Domain Method. *IEEE Transactions on Antennas and Propagation*. 1990, 38(7):1059–1068.
- [49] Yurkin, M. A. and Hoekstra, A. G.: The Discrete Dipole Approximation: An Overview and Recent Developments. *Journal of Quantitative Spectroscopy & Radiative Transfer*. 2007, 106:558–589.
- [50] Yurkin, M. A., Hoekstra, A. G., Brock, R. S., and Lu, J. Q.: Systematic Comparison of the Discrete Dipole Approximation and the Finite Difference Time Domain Method for Large Dielectric Scatterers. *Optics Express*. 2007, 15(26):17902–17911.
- [51] Purcell, E. M. and Pennypacker, C. R.: Scattering and Absorption of Light by Nonspherical Dielectric Grains. *Astrophysical Journal*. 1973, 186:705–714.
- [52] Yurkin, M. A., Maltsev, V. P., and Hoekstra, A. G.: Convergence of the Discrete Dipole Approximation. I. Theoretical Analysis. *Journal of the Optical Society of America A*. 2006, 23(10):2578–2591.
- [53] Yurkin, M. A. and Hoekstra, A. G.: The Discrete-Dipole-Approximation Code ADDA: Capabilities and known limitations. *Journal of Quantitative Spectroscopy & Radiative Transfer*. 2011, 112:2234–2247.
- [54] Draine, B. T. and Flatau, P. J.: Discrete-Dipole Approximation for Scattering Calculations. *Journal of the Optical Society of America A*. 1994, 11(4):1491–1499.
- [55] Mc Donald, J., Golden, A., and Jennings, S. G.: OpenDDA: A Novel High-Performance Computational Framework for the Discrete Dipole Approximation. *International Journal of High Performance Computing Applications*. 2009, 23:42–61.
- [56] Loke, V. L. Y. and Mengüç, M. P.: Surface Waves and Atomic Force Microscope Probe-Particle Near-Field Coupling: Discrete Dipole Approximation with Surface Interaction. *Journal of the Optical Society of America A*. 2010, 27(10):2293–2303.

- [57] Hoekstra, A. G. and Sloot, P. M. A.: New Computational Techniques to Simulate Light Scattering from Arbitrary Particles. *Particle & Particle Systems Characterization*. 1994, 11(3):189–193.
- [58] Yurkin, M. A., Maltsev, V. P., and Hoekstra, A. G.: The Discrete Dipole Approximation for Simulation of Light Scattering by Particles Much Larger than the Wavelength. *Journal of Quantitative Spectroscopy & Radiative Transfer*. 2007, 106:546–557.
- [59] Yurkin, M. A. and Hoekstra, A. G.: *User Manual for the Discrete Dipole Approximation Code ADDA v. 1.0*. [online]. 2010. 54 p.
http://a-dda.googlecode.com/svn/tags/rel_1.0/doc/manual.pdf, [visited 2015-03-21].
- [60] Garcia, M. A.: Surface Plasmons in Metallic Nanoparticles: Fundamentals and Applications. *Journal of Physics D: Applied Physics*. 2011, 44(28):283001.
- [61] Ordal, M. A., Long, L. L., Bell, R. J., Bell, S. E., Bell, R. R., Alexander, Jr., R. W., and Ward, C. A.: Optical Properties of the Metals Al, Co, Cu, Au, Fe, Pb, Pt, Ag, Ti, and W in the Infrared and Far Infrared. *Applied Optics*. 1983, 22(7):1099-1120.
- [62] Ligmajer, F.: *Ordered and Disordered Arrays of Colloidal Nanoparticles for Biomolecule Detection*. [Master thesis]. Brno: VUT, FSI, 2013. 61 p.
- [63] Ling, L., Huang, L., Fu, J., Guo, H., Li, J., Ou-Yang, H. D., and Li, Z.-Y.: The Properties of Gold Nanospheres Studied with Dark Field Optical Trapping. *Optics Express*. 2013, 21(5):6618–6624.
- [64] Ashkin, A.: Acceleration and Trapping of Particles by Radiation Pressure. *Physical Review Letters*. 1970, 24(4):156–159.
- [65] Ashkin, A.: Trapping of Atoms by Resonance Radiation Pressure. *Physical Review Letters*. 1978, 40(12):729–732.
- [66] Ashkin, A., Dziedzic, J. M., Bjorkholm, J. E., and Chu, S.: Observation of a Single-Beam Gradient Force Optical Trap for Dielectric Particles. *Optics Letters*. 1986, 11(5):288–290.
- [67] Ashkin, A.: Forces of a Single-Beam Gradient Laser Trap on a Dielectric Sphere in the Ray Optics Regime. *Biophysical Journal*. 1992, 61(2):569–582.

- [68] Lock, J. A.: Calculation of the Radiation Trapping Force for Laser Tweezers by Use of Generalized Lorenz-Mie Theory. II. On-Axis Trapping Force. *Applied Optics*. 2004, 43(12):2545–2554.
- [69] Koehler, A.: New Method of Illumination for Photomicrographical Purposes. *Journal of the Royal Microscopical Society*. 1894, 14(2):261–262.
- [70] Czerny, M. and Turner, A. F.: Über den Astigmatismus bei Spiegelspektrometern. *Zeitschrift für Physik*. 1930, 61(11-12):792–797.
- [71] Price, R. L. and Jerome, W. G. J.: *Basic Confocal Microscopy*. New York: Springer, 2011. 302 p. ISBN 0-387-78174-9.
- [72] Thermo Scientific [online]. <http://www.thermoscientific.com>, [visited 2015-05-21].
- [73] BBI Solutions [online]. <http://www.bbisolutions.com>, [visited 2015-05-18].
- [74] Mätzler, Ch.: *MATLAB Functions for Mie Scattering and Absorption*. [online]. 2002. 18 p. <http://omlc.org/software/mie/maetzlermie/Maetzler2002.pdf>, [visited 2015-05-22].
- [75] Palik, E. D.: *Handbook of Optical Constants of Solids*. London: Academic Press, 1997. 999 p. ISBN 0-125-44423-0.
- [76] Ungureanu, C., Rayavarapu, R. G., Manohar, A., and Leeuwen, T. G. van: Discrete Dipole Approximation Simulations of Gold Nanorod Optical Properties: Choice of Input Parameters and Comparison with Experiment. *Journal of Applied Physics*. 2009, 105:102032.
- [77] Nikoobakht, B. and El-Sayed, M. A.: Preparation and Growth Mechanism of Gold Nanorods (NRs) Using Seed-Mediated Growth Method. *Chemistry of Materials*. 2003, 15(10):1957–1962.
- [78] Optical Data from Sopra S.A. [online]. <http://www.sspectra.com/sopra.html>, [visited 2015-05-19].
- [79] Sigma-Aldrich Co. [online]. <http://www.sigmaaldrich.com>, [visited 2015-05-19].
- [80] Trojek, J., Chvátal, L., and Zemánek, P.: Optical Alignment and Confinement of an Ellipsoidal Nanorod in Optical Tweezers: A Theoretical Study. *Journal of the Optical Society of America A*. 2012, 29(7):1224–1236.

LIST OF ABBREVIATIONS

ADDA	Amsterdam Discrete Dipole Approximation
CAS	Czech Academy of Science
CGS	Centimetre–Gram–Second
CTAB	hexadecyltrimethylammonium bromide
CTU	Czech Technical University
DDA	Discrete Dipole Approximation
FDTD	Finite-Difference Time-Domain
LM	Longitudinal Mode
LSP	Localized Surface Plasmon
LSPP	Localized Surface Plasmon Polariton
SEIRA	Surface-Enhanced Infrared Absorption Spectroscopy
SEM	Scanning Electron Microscope
SERS	Surface-Enhanced Raman Scattering
SPP	Surface Plasmon Polariton
TM	Transversal Mode